




# Dusp26 phosphatase regulates mitochondrial respiration and oxidative stress and protects neuronal cell death

Binnur Eroglu<sup>1</sup> · Xiongjie Jin<sup>1</sup> · Sadiki Deane<sup>1,2</sup> · Bahadır Öztürk<sup>1,3</sup> · Owen A. Ross<sup>4</sup> · Demetrius Moskophidis<sup>1,5</sup> · Nahid F. Mivechi<sup>1,6,7</sup> 

Received: 19 October 2021 / Revised: 4 January 2022 / Accepted: 21 January 2022 / Published online: 21 March 2022  
© The Author(s), under exclusive licence to Springer Nature Switzerland AG 2022

## Abstract

The dual specificity protein phosphatases (Dusps) control dephosphorylation of mitogen-activated protein kinases (MAPKs) as well as other substrates. Here, we report that Dusp26, which is highly expressed in neuroblastoma cells and primary neurons is targeted to the mitochondrial outer membrane via its NH<sub>2</sub>-terminal mitochondrial targeting sequence. Loss of Dusp26 has a significant impact on mitochondrial function that is associated with increased levels of reactive oxygen species (ROS), reduction in ATP generation, reduction in mitochondria motility and release of mitochondrial HtrA2 protease into the cytoplasm. The mitochondrial dysregulation in dusp26-deficient neuroblastoma cells leads to the inhibition of cell proliferation and cell death. In vivo, Dusp26 is highly expressed in neurons in different brain regions, including cortex and midbrain (MB). Ablation of Dusp26 in mouse model leads to dopaminergic (DA) neuronal cell loss in the substantia nigra par compacta (SNpc), inflammatory response in MB and striatum, and phenotypes that are normally associated with Neurodegenerative diseases. Consistent with the data from our mouse model, Dusp26 expressing cells are significantly reduced in the SNpc of Parkinson's Disease patients. The underlying mechanism of DA neuronal death is that loss of Dusp26 in neurons increases mitochondrial ROS and concurrent activation of MAPK/p38 signaling pathway and inflammatory response. Our results suggest that regulation of mitochondrial-associated protein phosphorylation is essential for the maintenance of mitochondrial homeostasis and dysregulation of this process may contribute to the initiation and development of neurodegenerative diseases.

**Keywords** Dusp26 · p38 · Dopaminergic neurons · LRRK2 · Mouse model · Neurodegeneration

---

Binnur Eroglu and Xiongjie Jin contributed equally to this work.

---

✉ Demetrius Moskophidis  
dmoskofidis@augusta.edu

✉ Nahid F. Mivechi  
nmivechi@augusta.edu

Binnur Eroglu  
berolgu@augusta.edu

Xiongjie Jin  
xjin@augusta.edu

Sadiki Deane  
sadiki.deane@gmail.com

Bahadır Öztürk  
bahadirozturk@selcuk.edu.tr

Owen A. Ross  
Ross.Owen@mayo.edu

<sup>2</sup> Present Address: Department of Internal Medicine, University of Utah, Salt Lake City, Utah, USA

<sup>3</sup> Present Address: Medical Biochemistry Department, Selcuk University Medical Faculty, Konya, Turkey

<sup>4</sup> Mayo Clinic, 4500 San Pablo Rd., Jacksonville, FL 32224, USA

<sup>5</sup> Department of Medicine, Medical College of Georgia at Augusta University, 1120 15th St., CN3153, Augusta, GA 30912, USA

<sup>6</sup> Departments of Radiation Oncology, Medical College of Georgia at Augusta University, 1120 15th St., CN3153, Augusta, GA 30912, USA

<sup>7</sup> Charlie Norwood VAMC, One Freedom Way, Augusta, GA 30904, USA

<sup>1</sup> Molecular Chaperone Biology, Georgia Cancer Center, Medical College of Georgia at Augusta University, 1120 15th St., CN3153, Augusta, GA 30912, USA

## Introduction

Reversible phosphorylation of proteins by protein tyrosine kinases (PTKs) and tyrosine phosphatases (PTPs) is a key mechanism for signal transduction and regulation of a broad sets of physiological processes. Abnormal protein phosphorylation plays a critical role in the initiation and development of number of diseases, such as cancer, neurodegeneration, diabetes and immune deficiencies [1, 2]. Compared to the relatively well studied PTKs, the regulation and function of many PTPs remain elusive. More than one hundred PTPs in the human genome have been identified and have been grouped into four subfamilies. Class-I constitutes the majority of these proteins. Dual specificity protein phosphatases (Dusps) are a subgroup of the class-I PTP superfamily. Unlike the classical PTPs, Dusps can dephosphorylate both tyrosine and serine/threonine residues as well as other substrates (e.g., lipids). A group of 20 Dusps with highly conserved active site domains have been classified as atypical Dusps (aDusps) [2, 3]. The catalytic domains of aDusps are analogous to MAP-kinase phosphatases (MKPs) and, therefore, they are studied mainly in MAPK regulation [2, 4–6]. Dusp26/MKP8 is an atypical Dusp containing a conserved catalytic domain (residues 61–211) and an N-terminal region (residues 1–60), but lacks a substrate binding domain that is normally present in some Dusp family members. Dusp26 has been shown to regulate p38 and ERK1/2 activities [7–9]. In addition, Dusp26 has been detected in complexes with adenylate kinase 2 (AK2) modulating the activity of the Fas-associated protein with death domain (FADD) [10]. Dusp26 dephosphorylation of FADD at S<sup>191</sup> has a role in proliferation and is independent of its role in apoptosis. Studies also indicate that Dusp26 is a p53 phosphatase in neuroblastoma cells, and its inhibition leads to p53-mediated cell death [11, 12]. Through modulation of JNK activity, Dusp26 also has been shown to stimulate generation of Amyloid- $\beta$ 42 by promoting amyloid precursor protein (APP) processing under hypoxic conditions [13]. Dusp26 expression has also been detected in the neuroendocrine tissues and its activity is upregulated by NGF in PC12 cells [14]. Dusp26 enhances cell to cell contact through dephosphorylation of Kap3, which is a component of Kif3 motor complex [15]. More recently, Dusp26 was shown to protect against ROS-induced damage to renal tissue, which occurred through activation of MAPKs [16]. Dusp26 exhibits loss of heterozygosity in different tumor types and regulates neuronal cell proliferation [12, 14, 17, 18].

Recent studies demonstrate that reversible phosphorylation of mitochondrial proteins is a major mechanism for mitochondria response to various stimuli [19]. Indeed, up to 40% of mitochondrial proteins are phosphorylated. More than 30 protein kinases and phosphatases, including some

Dusps family members (Dusp18 and Dusp21), have been found to be associated with the mitochondria [20–25]. Even though many protein kinases and phosphatases do not translocate into the mitochondria, they do regulate protein phosphorylation on the outer mitochondria membrane (OMM), thus regulating signaling to and from the mitochondria often affecting mitochondria and cellular functions. These proteins include phosphorylation and regulation of PINK1, LRRK, and Bcl2 [26]. The dysregulation of the mitochondrial associated reversible phosphorylation leads to various cellular impairments including cell death. One major detrimental consequences of dysfunctional mitochondria is the enhanced ROS production. Depending on cell type, microenvironment and the origin of ROS, signaling induced by ROS may result in both normal physiological and pathophysiological effects. Due to the high oxygen demand and rich lipid content, cells in the CNS are specifically susceptible to ROS-induced killing. Numerous studies have demonstrated that ROS plays a central role in a common pathophysiology of neurodegenerative diseases such as Parkinson's disease (PD), Alzheimer's disease (AD) and Huntington's disease (HD) [27–29]. The mechanisms underlying cellular ROS increase that induce neurodegenerative diseases is likely due to the aberrant signaling and mitochondrial damage.

The NH<sub>2</sub>-terminal of Dusp26 protein sequence contains a putative mitochondrial targeting sequence. Coincidentally, previous studies suggest that Dusp26 is highly expressed in CNS neurons that have high mitochondrial content and oxygen consumption, while there is relatively low or no expression in other tissues [3]. These data indicate that Dusp26 may play a role in regulating mitochondrial function. In the current study, we show that Dusp26 is located on the OMM. Loss of Dusp26 in SH-SY5Y neuroblastoma cells impairs mitochondrial function, suppresses cell growth, increases cell death, and its disruption in mice leads to comparable mitochondrial defects as observed in SH-SY5Y cells, and death of midbrain (MB) dopaminergic (DA) neurons. The underlying mechanism of neuronal death in *dusp26*<sup>-/-</sup> brain is associated with an increase in the mitochondrial ROS and inflammatory response with concurrent activation of p38/MAPKs.

## Materials and methods

### Animal care and generation of mice deficient in the *dusp26* gene

All experiments with mice were approved by the Augusta University Institutional Animal Care and Use Committee (IACUC) in compliance with National Institutes of Health (NIH) guidelines. To generate *dusp26*-deficient mice, a BAC clone (RP24-120P2) containing the *dusp26* gene was used to

construct the targeting vector. A 5.3-kb proximal, and a 2.7-kb distal fragment with homology to murine *dusp26* gene was amplified by PCR using primers: forward (F), 5'-CCG CTCGAGCATGGTGCAGGTAGAGCTGA-3' (XhoI restriction enzyme site is underlined), reverse (R), 5'-CCG AAGCTTTTCAAGGTGGCAGGAACTGT-3' (HindIII restriction enzyme site is underlined) and F, 5'-ATAAGA ATGCGGCCGCGTTTGGGGGTTTTTGGTTTT-3' (NotI restriction enzyme site is underlined), R, CCGCTCGAGGGGCACG-TGACATTATACCC (XhoI restriction enzyme site is underlined), respectively. The PCR amplified fragments were digested by XhoI/HindIII (proximal fragment) and NotI/XhoI (distal fragment), and cloned into pBluescript plasmids. The sequences of the PCR amplified DNA fragments were confirmed by Sanger sequencing. The LacZ-neomycin cassette was used to introduce a LacZ reporter gene and positive selection marker (neomycin) into the *dusp26* targeting vector [30]. The neomycin gene was flanked by two Cre recombinase recognition sequences (LoxP) to allow removal of the neomycin gene in the mutant mice. The 5.3-kb proximal DNA fragment, LacZ-neomycin cassette and the 2.7-kb distal fragment were subcloned into the  $\lambda$ DASHII-254-2TK phage DNA vector at XhoI site to flank the targeting vector with 2 thymidine kinase (TK) genes, which were used as a negative selection marker [30]. The vector was packaged into the phage vector and the positive phage clones were selected. The positive phage DNA was digested by SalI to release the final vector that contained the targeting vector and the 2TK genes. The final targeting vector contained the *dusp26* gene in which a 742-bp DNA fragment next to ATG start codon of the *dusp26* gene was deleted. This deletion results in DNA reading-frame shift and creates a stop codon. The lacZ reporter gene followed the *dusp26* start codon (ATG). The targeting vector was linearized with SalI enzyme digestion and was electroporated into embryonic stem (ES) cells (D3; Incite Genomics, Genome Systems). ES cells were cultured in the presence of neomycin (200  $\mu$ g/ml) and ganciclovir (2 mM), and resistant clones were selected and expanded. Genomic DNA was isolated from the resistant clones and subjected to Southern blot analysis following BglII enzyme digestion. The probe used in the Southern blotting analysis was amplified by the following primer sets: F, 5'-AAGGGTGCTGCTGTCTCC TA-3' and R, 5'-GTAGCGGATCTGCTCACTCC-3'. Four ES clones were positively identified to contain the mutant *dusp26* gene by a homologous recombination event. Two positive ES cell clones were microinjected into 129SvEv blastocysts and germline transmitting chimeric mice were generated. Germ line transmission of the mutant allele was verified by Southern blotting and PCR of tail DNA using the following primer sets: P1: 5'-AGCCCATCATCACTGAAA CC-3' and P2: 5'-AAAACCAAAAACCCCCAAAC-3' for wild-type allele (817 bp), and P3: 5'-TAGCCTTGCCTTCTC

TCAGC-3' and P4: 5'-GACAGTATCGGCCTCAGGAA-3' for the mutant allele (412 bp).

## Plasmids and transfection

The plasmids encoding human Dusp26 (C-terminal Myc-Flag-tagged) was purchased from Origene (RC200202). The Flag-Dusp26 was generated previously [7]. The Myc-Pink1, WT LRRK2 and LRRK2 mutant constructs (Myc-tagged) were gift from Dr. Mark Cookson (NIH/NIA). Flag-MKK6, WT V5-His-LRRK2, His-LRRK2 G2019S and R1441G mutants were purchased from Addgene. The plasmids encoding Dusp26-EGFP deletion mutants were constructed in pcDNA3. HEK293T cells were cultured in DMEM with 10% heat inactivated FCS. Plasmids were transfected into cells using Continuum Transfection Reagent (Gemini Bioproducts). Cells were incubated for 48 h to allow gene expression before use.

The two specific Dusp26 targeting sgRNA (#1: F CAC CGCCTCGGGCGTGCCTCGCCAC, R: AAACGTGGC GAGGCACGCCCCGAGGC; #2 F: AAACGGTAACTG GCTTTGGGCTTCC, R: CACCGGAAGCCCCAAAGCC AGTTACC) were ligated into lentiCRISPRv2 (#52961, Addgene). The lentivirus-containing Dusp26 sgRNAs were produced in 293 cells following a standard protocol (addgene.com). Briefly, the plasmids together with lentiviral packaging plasmids pLP1, pLP2, pLP/VSVG (Invitrogen, K497500) were transfected into 293 cells using polyethylenimine (PEI). The virus was harvested 48 h post transfection. The Dusp26 knockout cells were selected with puromycin followed by immunoblotting and DNA sequencing of multiple clones to identify Dusp26 knockout lines (Fig. S1).

## Western blotting and immunoprecipitation

For western blotting analyses, cells or tissues were lysed in RIPA buffer (50 mM Tris/HCl, pH7.5, 1% NP-40, 0.5% sodium deoxycholate, 0.1% SDS, 150 mM NaCl) including protease inhibitor cocktail (Thermo Scientific). The supernatant was used for western blotting using equal amounts of protein (30  $\mu$ g) [30]. For immunoprecipitation, 1 mg of cell lysate was precleared with 10  $\mu$ l of Protein-A-Agarose for 1 h at 4  $^{\circ}$ C. 800  $\mu$ g of precleared supernatant was incubated with the primary antibody (anti-Myc, anti-Flag, etc.) at 4  $^{\circ}$ C overnight. 25  $\mu$ l of Protein A agarose was added and incubated at 4  $^{\circ}$ C for 1–2 h. After centrifugation, the pellet was rinsed with RIPA buffer and the pellets were subjected to immunoblotting [30]. The following antibodies were used in this study: Santa Cruz Biotechnology: UQCRC2 (sc-292924), Myc (sc-789), p-p38 (sc-166182)( $\alpha$ ,  $\beta$ ,  $\gamma$ ), Tom20 (sc-11415),  $\beta$ -actin (sc-47778); Cell Signaling Technology: Cleaved caspase3 (9661), p38 MAPK (9212), p-ERK1/2 (4370), Hsp60 (12165), p53 (#2425) and p-p53 (#82530);

BD Transduction Lab: Xiap (610763), Cytochrome c (556433); ABClonal: HtrA2 (B8515); Epitomics: Hsc73/HSPA8 (1966-1); Biologend: Flag (902401); and GeneTex: Dusp26 (GTX109283).

### Isolation of cytoplasmic and mitochondrial fractions

Isolation of cytoplasmic and mitochondrial fractions from different mouse brain regions was performed as previously reported [31]. Briefly, freshly dissected brain regions were homogenized in 300  $\mu$ l of Buffer A (250 mM sucrose, 50 mM Tris-HCl pH 7.4, 5 mM MgCl<sub>2</sub>, protease and phosphatase inhibitors). Homogenized samples were centrifuged at 800g for 15 min at 4 °C. Pellet was discarded and the supernatant (S0) was centrifuged at 800g for 10 min at 4 °C. Nuclear fraction (S1) was discarded. The cytoplasmic fraction (supernatant S2) was centrifuged at 11,000g for 10 min at 4 °C. After centrifugation, the supernatant (S3) was used as the cytosolic fraction and the pellet (P3) was used as the mitochondrial fraction. The S3 fraction was precipitated in cold acetone for 2 h. After 12,000g centrifugation for 5 min, pellet was re-suspended in 200  $\mu$ l Buffer A and used as cytosolic fraction. Pellet (P3) was re-suspended in 200  $\mu$ l Buffer A and centrifuged at 12,000g for 10 min. Pellet (P4) that comprises the mitochondrial fraction was sonicated 5  $\times$  in 100  $\mu$ l buffer B (50 mM Tris-HCl pH 6.8, 1 mM EDTA, 0.5% Triton-X-100, protease and phosphatase inhibitors) on ice for 5 s. Protein concentration was determined using BCA reagent (Pierce).

Proteinase K protection assay was performed as described previously [32]. Briefly, isolated mitochondria (100  $\mu$ g) were incubated in Iso-osmotic (10 mM MOPS-KOH pH7.2, 250 mM sucrose, 1 mM EDTA), Hypo-osmotic (10 mM MOPS-KOH pH7.2, 1 mM EDTA) or membrane-perforated (10 mM Tris-HCl pH7.2, 1 mM EDTA, 1% Triton X-100) buffer and digested on ice with, or without addition of proteinase K (20  $\mu$ g/ml) for 20 min. The reaction was terminated with the addition of 20 mM PMSF. Samples were centrifuged at 10,000g for 15 min at 4 °C and were analyzed by western blotting.

### Transmission electron microscopy (TEM)

TEM analyses were performed at the high-resolution electron microscopy facility at Augusta University. Mid-brain regions containing SNpc were fixed in situ by perfusion with 2% glutaraldehyde in 0.1 M sodium cacodylate (NaCac) buffer (pH 7.4), post-fixed with 2% MoSO<sub>4</sub>, also in NaCac buffer, for 1 h. After dehydration, tissues were embedded in Epon-Araldite resin. Thin sections (70 nm) were cut on the MT-7000 ultramicrotome and collected on copper grids. Sections were stained with uranyl acetate and lead citrate and examined under a JEM-1200 EXII TEM (JEOL

USA Inc., Peabody, MA). Images were captured with an UltraScan 4000 CCD camera and First Light Digital Camera Controller (Gatan Inc., Pleasanton, CA). In parallel, sections were immunostained using TH antibody to ensure presence of TH-positive cells.

### Histology and immunohistochemistry (IHC) and stereology

Brain tissues were frozen in OCT. 7- $\mu$ m frozen tissue sections were fixed in 10% formalin for 10 min. Immunostaining was performed after blocking the tissues with 3% BSA in PBST (PBS plus tween-20). For paraffin embedded brain, tissues were fixed in 10% formalin, embedded in paraffin and 7  $\mu$ m tissue sections were de-paraffinized in xylene and rehydrated in a series of alcohol/water mixtures. Antigen retrieval was performed by placing the slides in 10 mM sodium citrate, pH 6 including 0.05% Tween-20 and steamed for 30 min. Tissue sections were then blocked in 3% BSA in PBS for 1 h at 25 °C and then incubated in primary antibody for 16 h at 4 °C. Antibody/antigen was detected with fluorescent-conjugated secondary antibody. Nuclei were stained with DAPI. For immunostaining analyses, all tissue sections were stained with the secondary antibody only as control for nonspecific staining. For detection of  $\beta$ -gal, LacZ staining of frozen tissue sections were carried out using X-Gal staining [30]. Image acquisition was performed on a Zeiss AxioVision Imager Fluorescent Microscope supported with an AxioCam HRC camera (Carl Zeiss Microimaging Inc.) using a 40 $\times$  objective lens (NA 0.75). The AxioVision REL 4.8 software was used for data analysis. The following antibodies were used for IHC staining: Abcam: Dusp26 (b96429); Dako: GFAP (Z0334); Millipore: NeuN (MAB377), TH (AB152); Wako; Iba1 (019-19741); Sigma: TH (T2928); Santa Cruz Biotech: p-p38 (sc-58480), ERK1 (sc-94); Bioss: 8-OHDG (bs1278R); Assay Biotech: HtrA2 (B8515); CUSABIO: pS142-HtrA2 (CSB-PA008883).

For stereology, an unbiased method was used to determine the total numbers of TH immune-positive neurons in the SNpc [33]. To quantify TH/Nissl-positive neurons, deeply anesthetized mice were perfused with PBS and then with 4% PFA and the brains were fixed in 4% PFA in PBS overnight and then placed in 30% sucrose solution and kept at 4 °C for 48 h. Briefly, coronal sections of the entire SN were collected (30  $\mu$ m thickness) using a sliding vibratome. After washing, every 4th MB sections covering the entire SN were immunostained using antibody to TH and Nissl counter stain. Tissue sections were blocked in PBS containing 10% goat serum and 0.3% Triton X-100 for 1 h at 25 °C. Tissue sections were immunostained and developed with Vectastain (Vector Lab). Using 100 $\times$  objective, total number of TH/Nissl-positive neurons in the SNpc and VTA were quantified by a computer-assisted image analysis

system [Olympus BX-51 microscope equipped with an XYZ computer-controlled motorized stage and an SIA-L9C Digital Camera (Scientific Instruments and Applications)] and counted using the Optical Fractionator probe of Stereo Investigator software (MicroBrightField, RRID:nif-0000-00110) [33]. TH/Nissl-positive neurons were quantified in the SNpc or Ventral Tegmental Area (VTA) using the formula that has been previously reported for this method [33].

### Neuronal culture and drug treatment

Neuronal cultures derived from the MB or STR/cortices were prepared as previously reported [30]. After dissection, brain tissue samples were dissociated and digested with Papain (Worthington). Tissue digestion was inhibited using trypsin inhibitor, and cells were plated on poly-D-lysine-coated plates or coverslips. Neurons were cultured for 2 h in Basal Eagle's medium supplemented with 5% heat-inactivated FCS. After attachment, neurons were cultured in 1% N2 supplement (Invitrogen). Neurons were used typically 2 days after isolation. Identity of neurons were confirmed by immunofluorescence analyses using NeuN or TH antibodies.

### Time-lapse live cell imaging and quantification

Primary MB DA neuronal cultures were prepared as noted above and plated in 35 mm glass bottom plates (MatTek Corporation) and cultured at 37 °C, 5% CO<sub>2</sub> for 2–4 days. Neurons were transfected with Mito-dsRed plasmid alone, or cotransfected with plasmids encoding LC3-GFP using Continuum Transfection reagent (Gemini). Transfected neurons were incubated for 22 h before imaging. Plates were placed in a Fluorescent Microscope (Keyence model BZ-X710) containing a 37 °C, 5%CO<sub>2</sub> incubation chamber. Mitochondrial movement was quantified by counting the percentages of moving mitochondria during the imaging time. Time-lapse movies were obtained continually in 3-s intervals for 180 s before or following addition of 40 μM Antimycin A. Imaging of mitochondria was performed with a 40× objective in axons of longer than 50 μm in length. In each case, single axon was selected for mitochondrial motility recording. Movie length was up to 120–180 min. Kymographs were generated using Kymo analyzer, an open-source Image J software [34]. Kymographs were then used to analyze mitochondria motility (velocity), percent time in motion and normalized run length. For each condition, more than 120 mitochondria in three separate cultures were analyzed. Data were averaged over at least  $n = 10$  axons and five transfections and statistical analyses was performed using Student's *t* test and data plots were performed using Microsoft Excel.

### Total RNA and cDNA preparation and RT-PCR

Total RNA was isolated from MB or STR using TRIZOL reagent (Invitrogen) and reverse transcribed using Iscript cDNA synthesis kit (Bio-Rad). RT-qPCR reaction was performed using iQ SYBR Green Supermix (Bio-Rad). Relative quantitative plots were constructed for quantity of RNA input and for each gene of interest. The RT-qPCR was performed using gene-specific primers. List of primers are as follows: SOD1, F: AACCAGTTGTGTTGTCAGGAC, R: CCACCATGTTTCTTAGAGTGAGG, SOD2, F: CAG ACCTGCCTTACGACTATGG, R: CTCGGTGGCGTT GAGATTGTT, iNOS F: TTCACCCAGTTGTGCATCGAC CTA, R: TCCATGGTCACCTCCAACACAAGA, TNF $\alpha$  F: GCCTCTTCTCATTCTGCTT, R: CACTTGGTGGTT TGCTACGA, IL1 $\beta$  F: CCAAGCAATACCCAAGAA, R: CATCAGAGGCAAGGAGGAAA, INF $\gamma$  F: AGGAAC TGGCAAAGGATGGTG, R: GTGCT-GGCAGAATTATT CTTATTG. DUSP1 F: GGATATGAAGCGTTTTTCGGCT, R: GGATTCTGCA-CTGTCAGGCA, DUSP2 F: GTGCTC TTCTGAGGTGGCATA, R: TGGGAGCACAAG-GCTTAA GCT, DUSP4 F: CTACCTCGGCAGTGCCTATC, R: GAC GGGGATGCACTTGTACT, DUSP5 F: TGGATGTGAAGC CCACCTCA, R CGCACTTGGATGCGTGGTAG., DUSP8 F CACGT-GGCGAGGAGCTGG., R AGGAAAGCTGGG CAGCTCT., DUSP10 F: CGCCTACTTG-ATGAAGCACA, R: AGGTTCCGGGGAAATAATTGG.

### Mitochondrial complex activity and respiration assays

Isolation of mitochondria from different brain regions was performed as described above. Complex I activity in the isolated mitochondria was measured using modified enzymatic assay [35]. OCR was measured using a XF96 Extracellular Flux Analyzer (Seahorse Bioscience). Cells were seeded on the collagen-coated XF96 plates at  $4 \times 10^4$  cells/well for the primary neurons and  $10^5$  cells/well for SH-SY5Y cells and cultured overnight, rinsed twice, and kept in 100 μl of XF medium for 1 h (non-buffered XF base medium containing 25 mM glucose, 2 mM L-glutamine, and 1 mM sodium pyruvate). Three OCR measurements were obtained under basal and upon sequential injection of oligomycin (2 μM), FCCP (2 μM) and rotenone (0.5 μM) plus antimycin A (0.5 μM). OCR values were calculated from 3-min measurement cycles. The OCR measurements were adjusted to amount of the protein.

### Native PAGE analyses of OXPHOS

To study mitochondrial complex formation, Native-PAGE was performed as previously described [36]. Briefly, mitochondria (50 μg) from different brain regions were isolated

and solubilized in digitonin (6 g/g digitonin/protein ratio) and separated on a 3–12% Native-PAGE Bis-Tris Gel System and processed for immunoblotting with an OXPHOS antibody cocktail (Thermo Fisher Scientific).

## Behavioral studies

The grasping test of muscular rigidity was determined as described previously [37]. Briefly, mouse was suspended by its forepaws on a metal rod (0.25 cm in diameter and 24 cm length) located 20 cm above the surface. The amount of time that the animal remained on the rod was recorded. Maximum test time was 60 s. For evaluating locomotor activity, age-matched WT and *dusp26*-deficient male mice were individually placed in Oxymax Clams metabolic cages (Columbus Instruments). Each mouse was subjected to a 12-h light and dark cycles. After acclimatization, 3 days of data were collected and analyzed using manufacturer's instruction. Physical activity was measured as XY total activity (all horizontal beam breaks in counts), XY ambulatory activity (minimum three different, consecutive horizontal beam breaks in counts) and Z activity (all vertical beam breaks in counts) [38]. Data were taken every 14 min throughout the light and dark cycles.

## Measurement of cell cycle, mitochondrial membrane potential ( $\Delta\Psi_m$ ) and ROS levels

For cell cycle measurements, cells were fixed with ice-cold methanol for 10 min. After washing with PBS, cells were stained with 50  $\mu\text{g/ml}$  propidium iodide solution contained 1  $\mu\text{g/ml}$  RNase A for 30 min at 25 °C. After rinses with PBS, cell cycle parameters were analyzed using flow cytometry. The TMRE (T669, 50 nM), Mitosox (M36008, 5  $\mu\text{M}$ ), and Dihydroethidium (DHE, 3  $\mu\text{M}$ ) (D11347) (Fisher scientific) were used to measure mitochondria membrane potential ( $\Delta\Psi_m$ ), mitochondrial ROS, and cellular ROS, respectively, using live cells following incubation for 30 min. Cells were rinsed with PBS, and analyzed by flow cytometry.

## Statistical analyses

All experiments were performed at least 2–3 times using multiple samples or with at least 4–9 male or female mice for each time point and genotype unless stated otherwise. Ages of mice are indicated in figures (m). The ages of mice were selected as relevant to the phenotype in question since young mice exhibited less severe phenotype in terms of presence of TH-positive DA neurons while aged mice exhibited additional phenotypes in terms of, e.g., inflammation, etc. Results between males and females were consistent. Multiple sections of tissues ( $n = 5\text{--}10$ ) from each mouse were analyzed for histological or IHC analysis. For statistical

analyses, data were expressed as mean  $\pm$  SEM and analyzed using a two-tailed unpaired Student's *t* test.  $p < 0.05$  was considered significant.

## Results

### Dusp26 is targeted to the OMM through its NH<sub>2</sub>-terminal targeting sequence

In the human mitochondrial protein database {MitoProteome (mitoproteome.org)}, Dusp26 is listed as a putative mitochondrial associated protein. To determine whether Dusp26 contains a subcellular targeting signal peptide sequence (MTS), we analyzed its NH<sub>2</sub>-terminal domain (1–60aa) using MitoProt software (<https://ihg.gsf.de/ihg/mitoprot.html>) [39]. We identified a potential MTS for Dusp26 to be located between amino acid residues 1–29. To further verify the subcellular location of Dusp26, we examined the cytoplasm and mitochondrial fractions prepared from HEK293 cells that ectopically expressed Dusp26 and a mitochondrial-associated protein Pink1, which was used as a positive control. Immunoblotting analyses indicate that similar to Pink1, the major portion of Dusp26 is also associated with the mitochondrial fraction as demonstrated by the expression of mitochondrial resident protein, Hsp60 (Fig. 1A) [40]. To determine the Dusp26 subcellular location in cells under physiological growth condition, we detected the endogenous Dusp26 in the mitochondrial fraction prepared from human neuroblastoma cell line SH-SY5Y or HEK293 cells. Consistently, the major portion of the endogenous Dusp26 was detected in the mitochondrial fraction (75% in HEK293 cells and 70% in SH-SY5Y cells) (Fig. 1B). The expression of  $\beta$ Actin and mitochondrial protein UQCRC2 indicate the purity of each fraction.

To verify that putative MTS that is located in the NH<sub>2</sub>-terminal (1–29 aa) is functional in cells, we generated plasmid constructs expressing 1–34 amino acid residues of Dusp26 fused to EGFP, amino acid residues 29–211 fused to EGFP, and the full-length Dusp26 (amino acid residues 1–211) fused to EGFP (Fig. 1C). Immunofluorescent analyses following transient transfection of vectors into HEK293 cells together with Mito-dsRed, which is an expression vector containing MTS fused to the red fluorescent protein (dsRed), revealed that the predicted MTS (amino acids 1–29) of Dusp26 is sufficient to generate a homogeneous mitochondrial staining (Fig. 1D). No colocalization of Dusp26 amino acid residues 29–211-EGFP with Mito-dsRed was observed as this protein appeared as a diffuse staining pattern (Fig. 1D). The full-length Dusp26 (aa1-211-EGFP) often aggregated and did not result in a clear expression pattern, perhaps due to the relatively large length of the fusion protein (Fig. 1D).

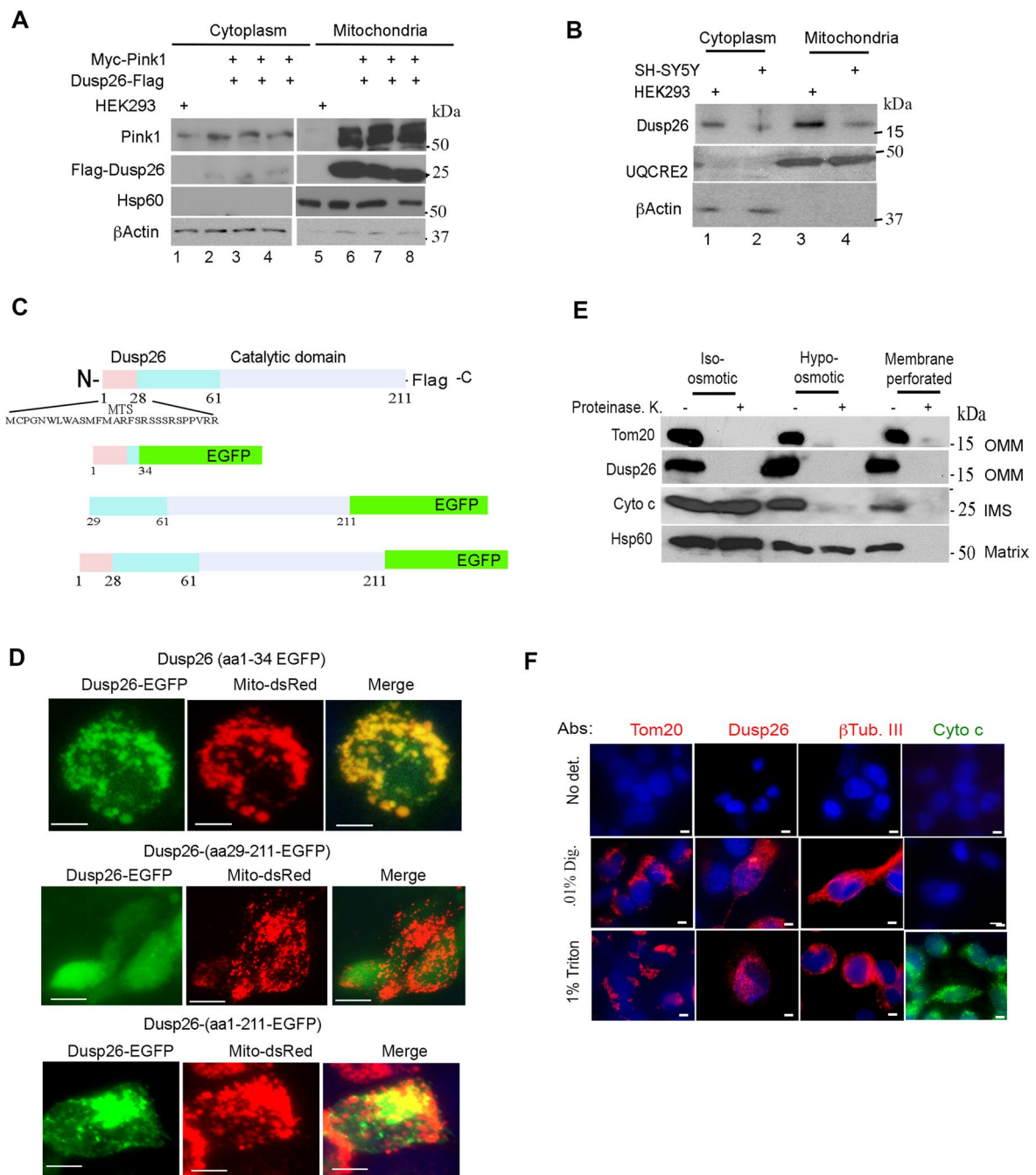


**Fig. 1** Dusp26 is targeted to the OMM via its NH<sub>2</sub>-terminal amino acid residues. **A** HEK293 cells were transiently transfected using control vector alone (lanes 1 and 5) or plasmids encoding Dusp26-Flag and Myc-Pink1 (lanes 2–4 and 6–8). Cytoplasm and mitochondrial fractions were analyzed by immunoblotting using antibody to Dusp26-Flag or Pink1. Hsp60 and  $\beta$ -actin were used to indicate mitochondria and cytoplasmic purity. **B** Cytoplasmic and mitochondrial fractions were isolated and immunoblotting analysis was performed to detect endogenous Dusp26 in HEK293 and SH-SY5Y cell lines. UQCRE2 and  $\beta$ -actin show purity of mitochondria and cytoplasmic fractions, respectively. Lanes 1–2, indicate cytoplasmic and lanes 3–4 indicate mitochondrial fractions. **C**, **D** Dusp26 domain structure and gene fragments that were fused to EGFP (C). HEK293 cells were transiently transfected using Mito-ds-Red and Dusp26 (aa1-

34)-EGFP, Dusp26 (aa29-211)-EGFP or Dusp26 (1–211)-EGFP constructs. Cells were cultured on a coverslip, fixed and examined by fluorescent microscope. Scale bar 5  $\mu$ m. **E** HEK293 cells transiently expressing Dusp26-Flag were untreated, or treated with proteinase K for 20 min (see “Materials and methods”) [32]. Following treatment, mitochondrial fractions were analyzed by immunoblotting using antibodies to the indicated proteins. **F** HEK293 cells were transiently transfected using Dusp26-Flag plasmids. Immunofluorescent analyses were performed with cells that were cultured on coverslips and were either untreated, treated with 0.01% digitonin or 1% triton. Cells were then stained with antibody to the indicated proteins. Scale bar 2  $\mu$ m. All experiments were performed three times and results were consistent

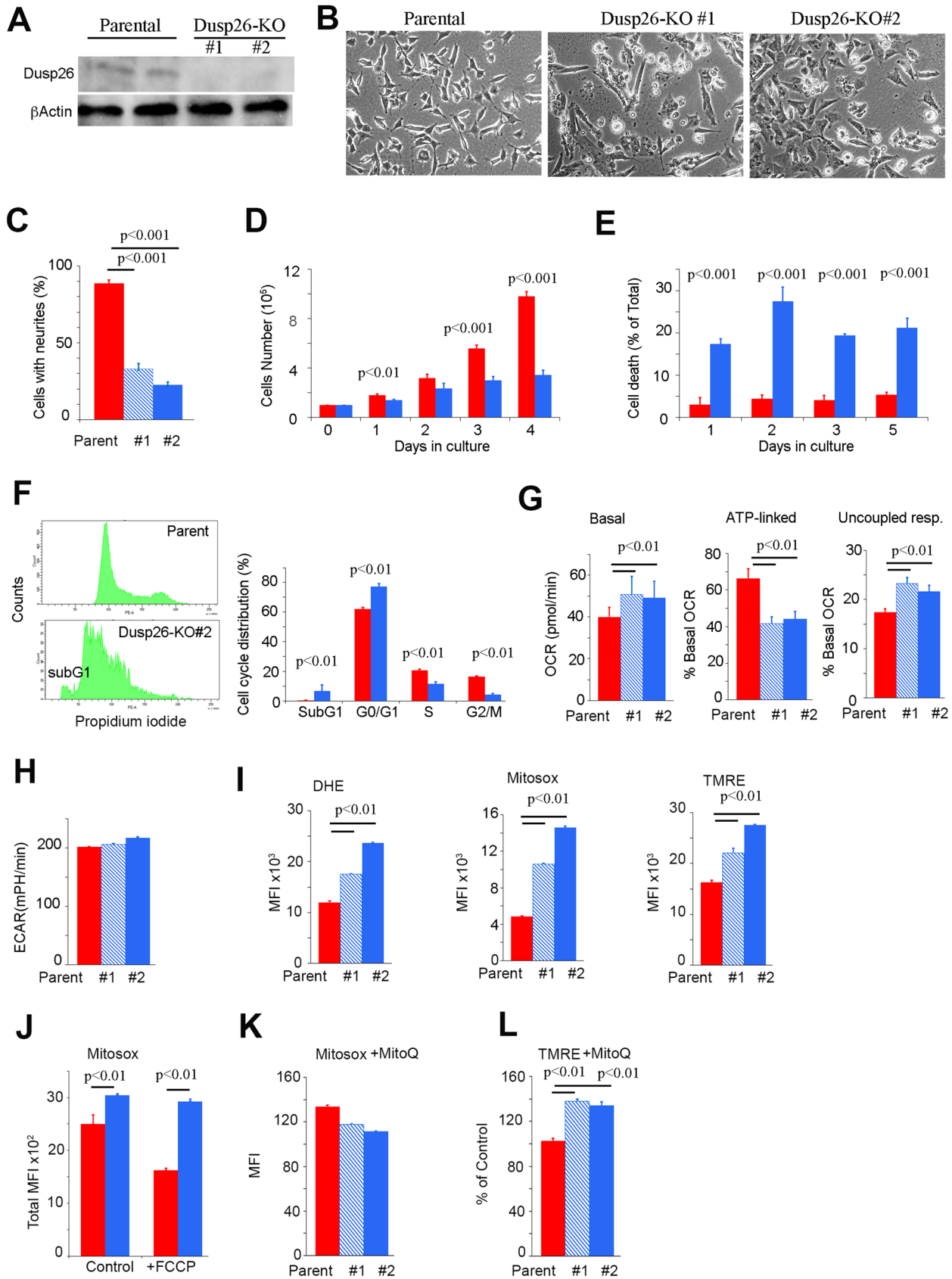




**Fig. 2** SH-SY5Y cells exhibit mitochondrial impairment following loss of Dusp26. **A** Dusp26 expression levels in parental and two Dusp26 deficient SH-SY5Y clones (#1 and #2) were determined by immunoblotting. The Dusp26-deficient cell lines were generated by targeting the exon 2 region of Dusp26 DNA using CRISPR/CAS9 system.  $\beta$ -actin is loading control. **B, C** Phase contrast images of parental and Dusp26-deficient SH-SY5Y cell lines #1 and #2. Loss of Dusp26 causes apparent cell morphological alteration. Quantification of the cells with neurites (**C**). 10–15 microscopic fields from independent cultures for each cell line were analyzed for the presence of neurites. **D, E** Quantification of cell proliferation and cell death.  $10^5$  parental and Dusp26-deficient cells (#2) were plated and cell number was determined at the indicated times (**D**). Cell death was determined by trypan blue exclusion in live cells (**E**). **F** Cell cycle analysis performed by propidium iodide staining followed by FACS analyses. The representative cell cycle histograms (left panel) and quantification of the data are presented (right panel).  $n=3$ /group. The experiments were repeated twice independently. **G** Oxygen consumption rate (OCR) of the parental and Dusp26-deficient SH-SY5Y cells was determined using XF96 Seahorse analyzer. The basal, ATP-linked and uncoupled respiration-linked OCR are presented. **H** Extracellular acidification rate (ECAR) of parental and Dusp26-deficient SH-SY5Y cells was determined using XF96 Seahorse analyzer. **I** The level of cellular ROS (left), mitochondrial ROS (middle), and  $\Delta\Psi_m$  (right) in parental and Dusp26-deficient SH-SY5Y cells were determined using DHE, mitosox and TMRE followed by FACS analyses. MFI (mean fluorescence intensity). **J** ROS in control and FCCP-treated parental and Dusp26-deficient cells was measured as in **I**. **K, L** The parental and Dusp26-deficient SH-SY5Y cells were treated with MitoQ to reduce ROS. The mitochondrial ROS and  $\Delta\Psi_m$  were measured as in **I**. All experiments were performed two times and in triplicates. In all relevant panels, red bars are the parental line and blue bars are Dusp26-KO clone #2 or as indicated in the panels and bars indicate mean  $\pm$  SEM,  $p$  values are indicated in the panels

To further determine the sub-mitochondrial location of Dusp26, we performed proteinase K protection assay [32]. The data indicate that Dusp26 is mainly associated with the OMM as does Tom20, a known OMM protein, while as expected Hsp60 and cytochrome *c* were detected in the matrix and the inner mitochondrial space (IMS), respectively [32] (Fig. 1E). To confirm whether Dusp26 is located in the outer side of the mitochondrial membrane, we performed immunofluorescence analyses where HEK293 cells expressing Dusp26 were treated with no detergent, where no antibody enters the cytoplasm, or treated with 0.01% digitonin, which allows antibody to enter the cytoplasm, or treated with 1% Triton-x-100, which permeabilizes all the cellular membranes [41]. The  $\beta$ -tubulin-III immunostaining was used as a positive control for the detergent treatment. No immunostaining for the indicated antibodies was observed when cells were treated with no detergent (Fig. 1F). Positive immunostaining of Tom20 and Dusp26 were observed, but not cytochrome *c*, when cells were treated with 0.01% digitonin. All the proteins, namely Tom20, Dusp26, and cytochrome *c* were positively stained when cells were treated with 1% Triton-x-100. These results indicate that Dusp26 is not located on the inner membrane or matrix of

the mitochondria (Fig. 1F). Taken together, above results suggest that Dusp26 protein is targeted to the OMM.

### Loss of Dusp26 impairs mitochondrial function and increases mitochondrial ROS in SH-SY5Y cells

The expression of Dusp26 is low in most normal human and mouse tissues and cell lines with the exception of CNS neurons and muscle cells (not shown and [3, 42, 43]). Dusp26 expression is also abundant in the human neuroblastoma cell lines including SH-SY5Y [3]. To investigate the function of Dusp26 in neuroblastoma cells, we knocked-out Dusp26 in SH-SY5Y cells using CRISPR/CAS9 technology. We generated 2 *dusp26*-deficient lines in two independent experiments. Deletion of Dusp26 in both cell lines were verified by immunoblotting (Fig. 2A). Deletion of Dusp26 altered SH-SY5Y cells' morphology and proliferation rate (Fig. 2B–D). The sizes of the *dusp26*-deficient cells appeared larger compared to parent line (Fig. 2B) and the neurites that normally appear in these cells were significantly reduced in number in *dusp26*-deficient cells compared to the parental cell line (Fig. 2B, C). In terms of the proliferation rate, *dusp26*-deficient cells exhibited doubling time that was reduced more than 50% compared to the parent cell line ( $45.1 \pm 5.8$  h vs  $28.6 \pm 3.7$  h) (Fig. 2D). Deletion of Dusp26 also increased cell death (18–27% within a 24-h period), while less than 5% of the cells in the parent line underwent cell death (Fig. 2E). Cell cycle analysis indicated that increased number of *dusp26*-deficient cells accumulate in the  $G_0/G_1$  phase compared to the parent line ( $77 \pm 3\%$  vs  $62 \pm 2\%$ ) (Fig. 2F), while more of the parent cells is in the S ( $12 \pm 1\%$  vs  $21 \pm 3\%$ ) or G2/M ( $4 \pm 1\%$  vs  $16 \pm 2\%$ ) phase. Taken together, the above results suggest that Dusp26 is required to maintain SH-SY5Y cell survival and proliferative capacity.

Given that Dusp26 protein is targeted to the OMM, we evaluated the mitochondrial function in *dusp26*-deficient SH-SY5Y cells and parental cells by examining mitochondrial respiration. Dusp26 deletion increased the mitochondrial respiration (basal OCR) (Fig. 2G); however, the ATP production was not increased correspondingly. The percentage of OCR-linked to ATP production in *dusp26*-deficient cells was significantly reduced (Fig. 2G), while the percentage of OCR linked to uncoupled respiration was significantly increased (Fig. 2G). Although these data suggest that loss of Dusp26 impairs mitochondrial ATP production capacity, the deletion of Dusp26 did not affect glycolysis in these cells relative to the parent line (Fig. 2H). Accompanied with the impairment of mitochondrial respiration, cellular and mitochondrial ROS levels measured by DHE and mitosox, respectively, significantly increased in *dusp26*-deficient cells compared to parent line (Fig. 2I). The mitochondria membrane potential ( $\Delta\Psi_m$ ) is associated with increased mitochondrial ROS production by slowing

down the mitochondria electron transport [44]. Interestingly,  $\Delta\Psi_m$  was significantly enhanced in *dusp26*-deficient cells (Fig. 2I). To test whether the increases in ROS levels results from the higher  $\Delta\Psi_m$  in *dusp26*-deficient cells, we treated cells with FCCP to dissipate  $\Delta\Psi_m$ . In the parental cells, as expected, FCCP treatment reduced mitochondrial ROS production measured by Mitosox (Fig. 2J). However, mitochondrial ROS production was not reduced following FCCP treatment in *dusp26*-deficient cells (Fig. 2J). On the other hand, treatment of cells with mitoQ, while reducing ROS levels, did not rescue the increases of  $\Delta\Psi_m$  in *dusp26*-deficient cells (Fig. 2K, L). These results suggest that the higher ROS production in *dusp26*-deficient cells is not due to the higher  $\Delta\Psi_m$ . Taken together, the above data indicate that Dusp26 deletion impairs mitochondrial homeostasis that leads to increased ROS generation, which may contribute to increase in cell death.

### Dusp26 is highly expressed in the CNS neurons

The regulatory function of Dusp26 on the mitochondria and the ROS generation and its selective expression in neurons suggest that Dusp26 may play an important role in the neuronal cell survival. Thus, to examine neuronal survival in vivo following loss of Dusp26, we generated a *dusp26*-deficient mouse model (*dusp26*<sup>-/-</sup>) where we disrupted the *dusp26* gene and placed the  $\beta$ -galactosidase ( $\beta$ -gal) gene under the control of the Dusp26 promoter elements (Fig. 3A). The targeted deletion of the *dusp26* gene was confirmed by Southern blotting and PCR (Fig. 3B). *Dusp26*<sup>-/-</sup> mice were fertile and born with the expected Mendelian frequency and did not exhibit any visible abnormality compared to wild-type (WT) littermates. As expected, IHC staining analyses of the brain tissue sections using antibodies specific to Dusp26 and NeuN, a neuronal cell marker, show that Dusp26 is expressed in the CNS neurons of WT mice and its expression is eliminated in the *dusp26*<sup>-/-</sup> mice (Fig. 3C). To evaluate Dusp26 expression pattern in the CNS, we tested the expression of  $\beta$ -gal in cultured neurons (Fig. 3D) and LacZ staining of multiple brain regions of *dusp26*<sup>+/ $\beta$ -gal</sup> mice (Fig. 3E). The data indicate that Dusp26 is expressed in cultured neurons and other cells derived from different regions of the brain including cortex and the midbrain (MB). Next, we further detected the Dusp26 expression using  $\beta$ -gal as a reporter marker in our mouse model. Although it has been reported that Dusp26 is highly expressed in heart and muscle cells using RT-qPCR, the  $\beta$ -gal staining indicates that Dusp26 is widely expressed in the CNS and retina (Fig. 3E), but not significantly in other tissues (not shown).

### Dusp26 loss reduces tyrosine hydroxylase (TH)-positive neurons in the MB

Next, we sought to investigate the function of Dusp26 in neuronal cells. We first quantified the neuronal cell number in the cortex and hippocampus, where the Dusp26 is expressed, by staining the brain tissue sections from aged WT and *dusp26*<sup>-/-</sup> mice with neuronal cell marker NeuN and  $\beta$ -tubulin III as well as Nissl. The total neuronal cell number in the cortex of *dusp26*<sup>-/-</sup> mice was comparable to that of WT mice (Fig. S2A and C). The  $\beta$ -tubulin-III immunostaining did not reveal significant alterations (Fig. S2B). We then determined the number of TH/Nissl-positive neurons in the MB/substantia nigra par compacta (SNpc) region. Interestingly, the number of TH/Nissl-positive neurons in the SNpc was significantly reduced in 2-month-, and more severely in 16-month-old *dusp26*<sup>-/-</sup> mice compared to WT mice (Fig. 4A, B). Immunostaining of WT brain tissue sections confirmed that Dusp26 is expressed in TH-positive neurons in the SNpc (Fig. 4C). Consistently, the immunoblot analyses of MB region also show significant reduction in the TH levels in *dusp26*<sup>-/-</sup> brain tissue extracts analyzed at 10 months of age (Fig. 4D). In the MB region, dopaminergic (DA) neurons comprise the majority of TH-positive neurons. DA neurons in the SN normally project into the dorsal striatum (STR) (caudate putamen, CPu) and the intensity of TH immunostaining is often reduced in the SN and STR in diseases such Parkinson's Disease (PD). We observed a reduction in the intensity of TH-immunoreactive axons in the dorsal STR in *dusp26*<sup>-/-</sup> mice compared to WT examined at 12 months of age (Fig. 4E). Taken together, these results indicate that loss of Dusp26 lead to a significant DA neuronal loss.

Motor deficit is one of the major features of DA neuronal impairment [45, 46]. Although we did not observe tremor and unstable posture in the *dusp26*<sup>-/-</sup> mice for up to 20 months of age (data not shown), we observed reduced physical activity in *dusp26*<sup>-/-</sup> mice. Both WT and *dusp26*<sup>-/-</sup> mice show comparable muscle strength (grip strength) at 4 months of age, but *dusp26*<sup>-/-</sup> mice exhibited reduction relative to WT at 20 months of age (Fig. 4F). Additionally, monitoring the physical activity of mice using OxyMax/Clams chambers along the *x*-, *y*- and *z*-axes indicated that *dusp26*<sup>-/-</sup> mice exhibited significantly reduced motor activity, as measured by *x*-total, *x*-ambulatory (AMB) or *Z*-total counts during the dark, and the 24-h period compared to WT (Fig. 4G). The differences during the light period, where mice are not overtly active, was not significant for the *X*-total. Taken together, the above results confirm that Dusp26 is expressed in the neuronal cell population and that the DA neurons are uniquely sensitive to Dusp26-loss.

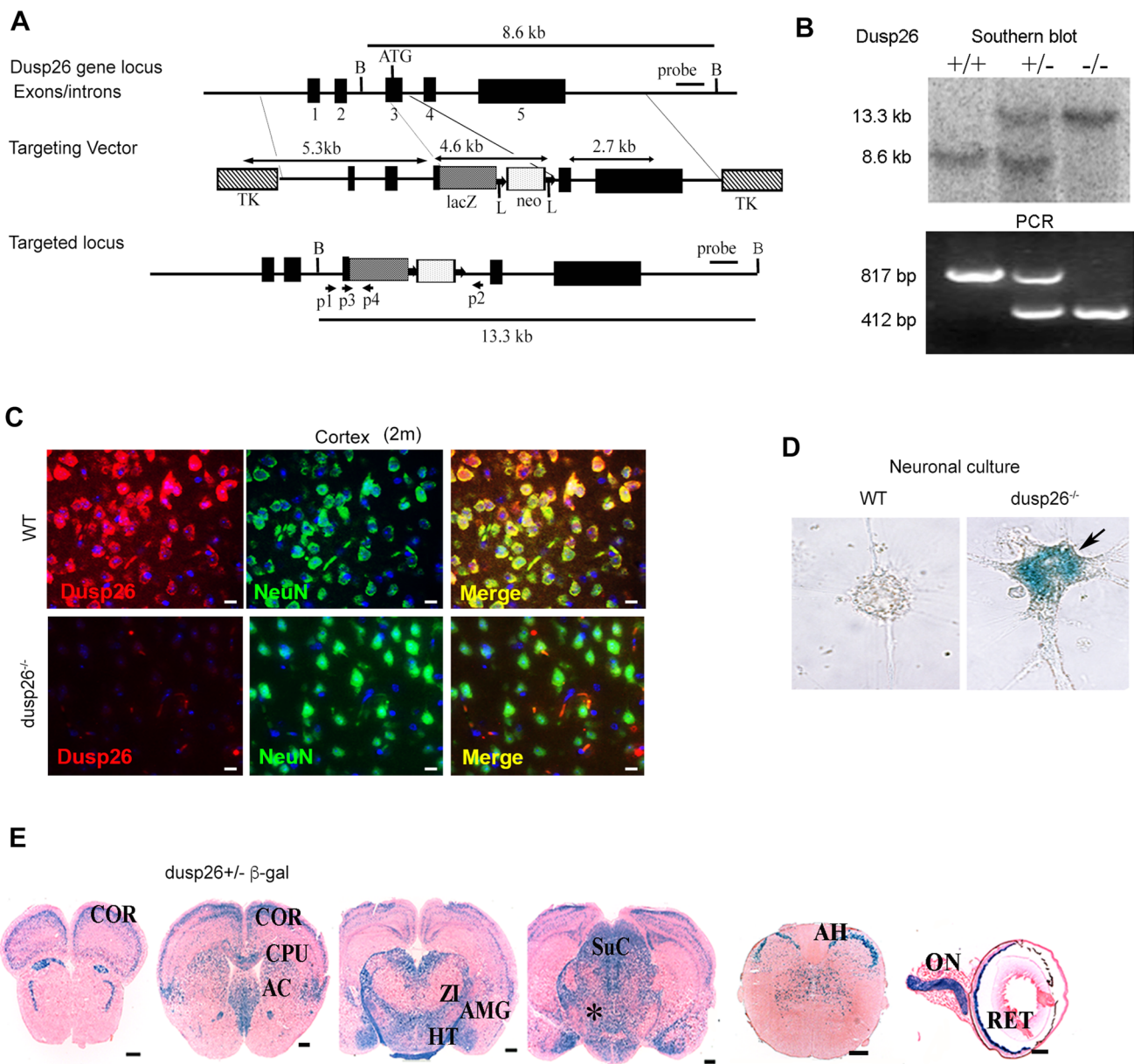


**Fig. 3** Generation of mice with the targeted deletion of the *dusp26* gene. **A** Genomic locus, targeting vector and targeted locus of the *dusp26* gene. p1, p2, p3 and p4 represent the location of the primers used to detect WT and mutant Dusp26 genes. Positions of the probe that was used to identify targeted ES clones are indicated. LacZ is the β-gal gene. Neo represents neomycin, and TK represents the thymidine kinase gene, which were used for positive and negative selection, respectively. Black boxes represent exons. **B** Southern blot and PCR analyses of tail DNA that were used to confirm the genotype of Dusp26 WT (+/+), heterozygous (+/-) and homozygous (-/-) mutant mice. kb=kilobase pairs; bp=base pairs. **C** IHC staining of

the cortical brain region of mice showing co-expression Dusp26 and NeuN. Nuclei were stained with DAPI. Scale bar 10 μm. **D** WT and *dusp26*<sup>-/-</sup> primary neuronal cell cultures were stained for the expression of β-gal (arrow shows positive β-gal staining). **E** Coronal brain tissue sections of the *dusp26*<sup>+/-β-gal</sup> mice stained to detect the β-gal expression. Dusp26 expression is apparent in the COR cortex, CPU caudate putamen, AC anterior commissure, ZI zona incerta, AMG amygdala, HT hypothalamus, SuC superior colliculus, AH anterior horn of the spinal cord, RET retina, ON optic nerve. \*midbrain. Scale bar 500 μm. All experiments were performed three times or with 5 mice/group, which included both males and females

### Loss of *dusp26* impairs mitochondrial function of primary neurons

As indicated above, we show that loss of Dusp26 impairs mitochondrial function and increases ROS production in

neuroblastoma cells. It is plausible that same detrimental processes occurs in DA neuron of *dusp26*<sup>-/-</sup> mice in vivo, leading to DA neuronal death. To test this hypothesis, we performed a series of experiments to determine the mitochondrial function in the neuronal cell population of WT

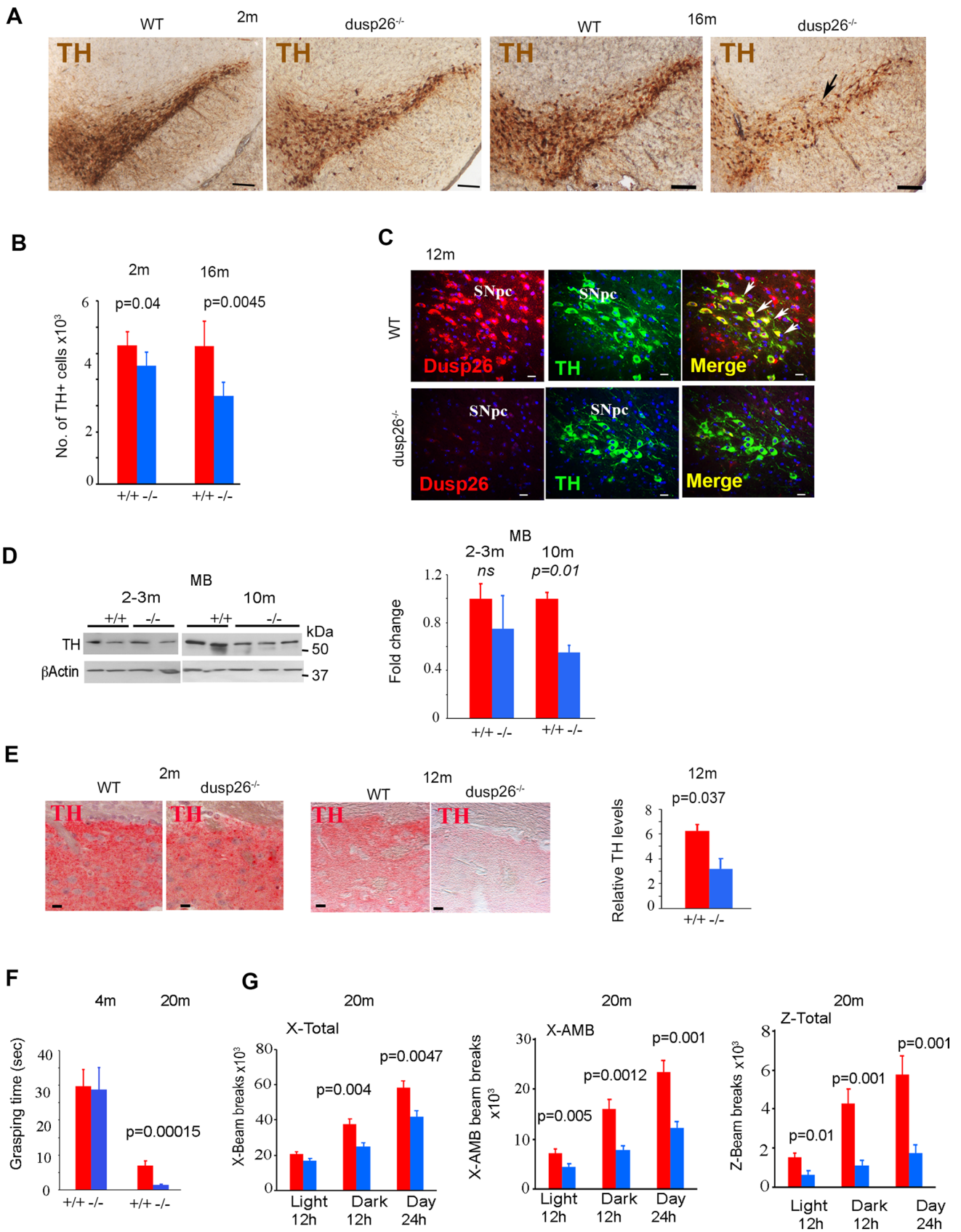


**Fig. 4** Loss of Dusp26 leads to death of DA neurons in SNpc. **A, B** Coronal sections of MB of 2- or 16-month-old mice (2 m and 16 m) immunostained with TH-specific antibody and developed using Vectastain (brown). Arrow indicates general area of loss of TH-positive cells. Scale bar 10  $\mu$ m. Quantification of TH/Nissl-positive neurons in SNpc using stereology (**B**).  $n=5$  mice per group. **C** Immunofluorescent staining of SNpc showing colocalization of TH and Dusp26 in both genotypes. Merged image shows colocalization of TH and Dusp26 in WT sample. DAPI is used to stain the nuclei.  $n=5$  mice. Scale bar 10  $\mu$ m. **D** Immunoblotting analyses of MB tissue lysates using antibody to TH. Quantification of the data is presented in the right panels.  $\beta$ -actin is used as loading control. 4–5 mice/group. **E** Coronal sections of the dorsal STR immunostained to detect TH and developed using fast-red. Bar 10  $\mu$ m. Quantification of the intensities of TH staining is presented in the right panel.  $n=5$  mice. **F** Muscle strength (measured by grasping test) of mice was analyzed at 4- and 20-months-of-age.  $n=9$  mice for WT and 14 mice for *dusp26*<sup>-/-</sup>. **G** Physical activity of WT and *dusp26*<sup>-/-</sup> mice at 20-months-of-age was analyzed in Oxymax/Clams monitored by infrared beam breaks. Total activity (X-TOTAL, walking, grooming), ambulatory activity (X-AMB, walking) and z-axis activity (Z-TOTAL, rearing) are presented. Data presented as light, dark and 24 h periods.  $n=9$  mice/group. In all relevant panels, bars indicate mean  $\pm$  SEM,  $p$  values are indicated in the panels. Red bars represent WT and blue bars represent *dusp26*<sup>-/-</sup> mice

and *dusp26*<sup>-/-</sup> mice. The deficiency in the capacity of mitochondrial respiration has been linked to the abnormalities observed in the MB DA neurons of some mouse models [47, 48]. Our data indicate that MB neurons deficient in the *dusp26* gene exhibit significantly reduced basal, maximal and ATP-related OCRs relative to WT (Fig. 5A). Consistent with this, reduction in the complex I (C-I) activity in the MB neurons following loss of the *dusp26* gene was also observed (Fig. 5B). Though impairing the function of mitochondrial respiratory complexes, loss of Dusp26 did not show significant effect on the assembly of respiratory complexes and their expression levels in the MB and STR analyzed by native PAGE electrophoresis (Fig. 5C). In addition, immunoblot analyses of mitochondrial fractions to detect representative C-I to C-V, namely NDUFA9, SDHA, UQCRC2, MT-CO1 and ATP5A protein levels showed no significant alterations in the respiratory complexes upon Dusp26 loss (data not shown). The expression levels of proteins involved in the mitochondria fusion and fission and proteins such as Parkin, which once activated leads to degradation of Mitofusion 2 (MFN2), DRP1 and OPA1, is comparable between WT and *dusp26*<sup>-/-</sup> isolated mitochondria from the brain tissue (Fig. 5D). The NDUFA9, a C-I subunit show the purity of the mitochondrial fraction.

To further assess mitochondrial structure, we examined the ultrastructure of the SNpc region of WT and *dusp26*<sup>-/-</sup> mice using TEM analyses. While WT MB region exhibited abundant normal mitochondria with having no evidence of any damage, the MB region of *dusp26*<sup>-/-</sup> mice while mostly intact and appeared normal (Fig. 5E, green arrows), also showed few cluster areas (an average of 2

clusters/TEM section) of damaged organelles. Within the clusters, there was evidence of intact or damaged mitochondria inside of autophagosomes, number of electron dense lamellar inclusion bodies and swollen vacuoles (Fig. 5E, red arrows) and number of structures similar to lysosomes (red \*). Quantification of the mitochondria length and aspect ratio (AR) revealed that among the healthy mitochondria in the *dusp26*<sup>-/-</sup> MB region compared to WT mice (presented in the upper panels of Fig. 5E), the mitochondria were significantly shorter and rounder (Fig. 5F).

As noted above, we did not observe any changes in the expression of Parkin substrates (MFN, OPA1 or DRP1), suggesting that Parkin likely was not activated following loss of Dusp26. Therefore, to further evaluate the state of the mitochondrial damage in cells in the MB region in vivo, we determined the level of another protease, namely the total and phosphorylated HtrA2 using immunostaining of SNpc sections from WT and *dusp26*<sup>-/-</sup> mice. HtrA2 is a mitochondrial protease whose expression is low under normal physiological conditions. Upon mitochondrial damage, HtrA2 is stabilized, released into the cytoplasm, phosphorylated by p38 on S<sup>142</sup> in a Pink1-dependent manner [49], leading to an increase in the degradation of specific cytoplasmic and mitochondrial substrates and subsequently can induce cellular apoptosis [49–53]. Immunostaining analyses of MB tissue sections of WT and *dusp26*<sup>-/-</sup> mice indicate significant increases in the levels of pS<sup>142</sup>-HtrA2 and total HtrA2 in the SNpc of *dusp26*<sup>-/-</sup> mice compared to WT mice, suggesting the presence of mitochondrial damage in *dusp26*<sup>-/-</sup> mice (Fig. 6A). Of note, there was an increase in HtrA2 colocalized with the TH-positive cells in the SNpc region in *dusp26*<sup>-/-</sup> mice (Fig. 6B). Furthermore, immunoblotting analyses using mitochondria and cytoplasmic fractions purified from the MB region indicate significant increases in the level of HtrA2 in the cytoplasmic fraction from cells in the MB region of *dusp26*<sup>-/-</sup> mice compared to WT mice (Fig. 6C), again suggesting that there are mitochondria damages in the neurons of *dusp26*<sup>-/-</sup> mice. The expression of Hsc70 and Hsp60 were used to indicate the purity of cytosolic and mitochondrial fractions, respectively (Fig. 6C). One of the known HtrA2 substrates is Xiap. Thus, we performed immunoblotting analyses to detect whether we can observe the degradation of this protein following loss of Dusp26 [54]. We observed reduced level of Xiap in the MB, but not in the cortex of aging *dusp26*<sup>-/-</sup> mice compared to WT mice, suggesting the enhanced HtrA2 activity in MB of *dusp26*<sup>-/-</sup> mice (Fig. 6D).

Another interesting alteration in the mitochondrial function that resulted from the loss of the *dusp26* gene in the neurons is the reduction in the mitochondrial movement. Carefully dissected and cultured MB neurons contained high numbers of DA neurons identified by TH expression using immunofluorescence staining analyses (Fig. 7A). Using

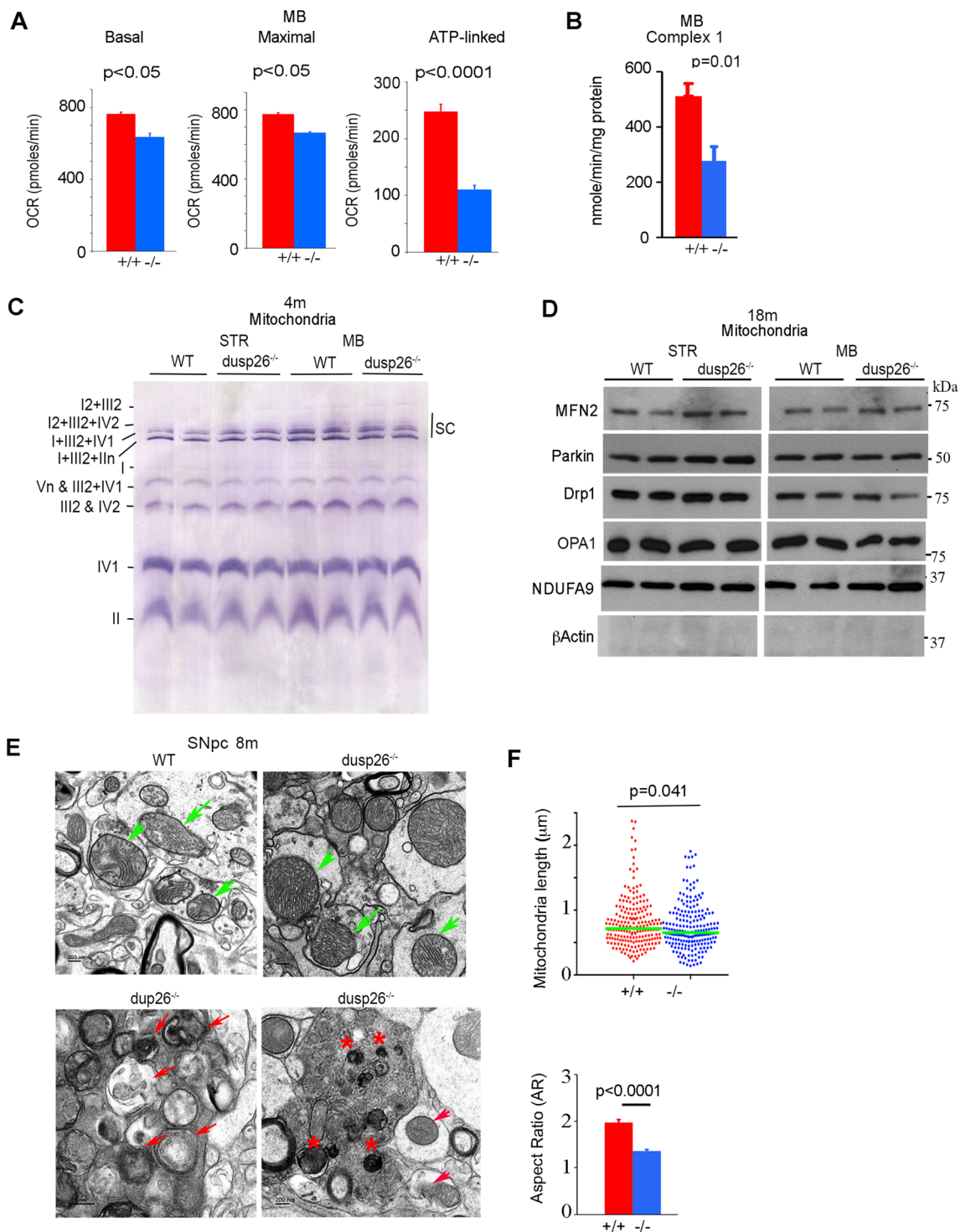


**Fig. 5** Mitochondrial impairment following loss of *Dusp26*. **A** OCR was measured in the primary MB neurons using XF96 Seahorse analyzer in the indicated genotypes. The basal, maximal and ATP-linked OCR are presented.  $n=16$ /group and two independent experiments. **B** MB mitochondrial fractions were used to determine complex I activity in the indicated genotypes.  $n=5$  mice. **C** Native-PAGE followed by immunoblot analyses using a mixture of OXPHOS antibodies showing mitochondria complexes (I–V) and respiratory super-complexes (SC). **D** Immunoblot analyses of mitochondrial fractions isolated from STR and MB using antibodies to the indicated proteins.  $\beta$ -actin is loading control.  $n=2$  experiments in duplicates. **E**, **F** TEM analyses of SNpc

region. To ensure the correct area was selected, consecutive sections were immunostained using antibody to TH (not shown). The green arrows represent healthy appearing mitochondria in both genotypes. In *dusp26*<sup>-/-</sup> TEM, which contained few clusters with aberrant organelles (the two panels below), there was evidence of intact or damaged mitochondria inside of autophagosomes, number of electron dense lamellar inclusion bodies and swollen vacuoles (red arrows) and number of structures similar to lysosomes (\*). Mitochondrial length and aspect ratios (AR) were determined in >200 mitochondria (**F**). In all relevant panels, bars are mean  $\pm$  SEM.  $p$  values are indicated in each panel

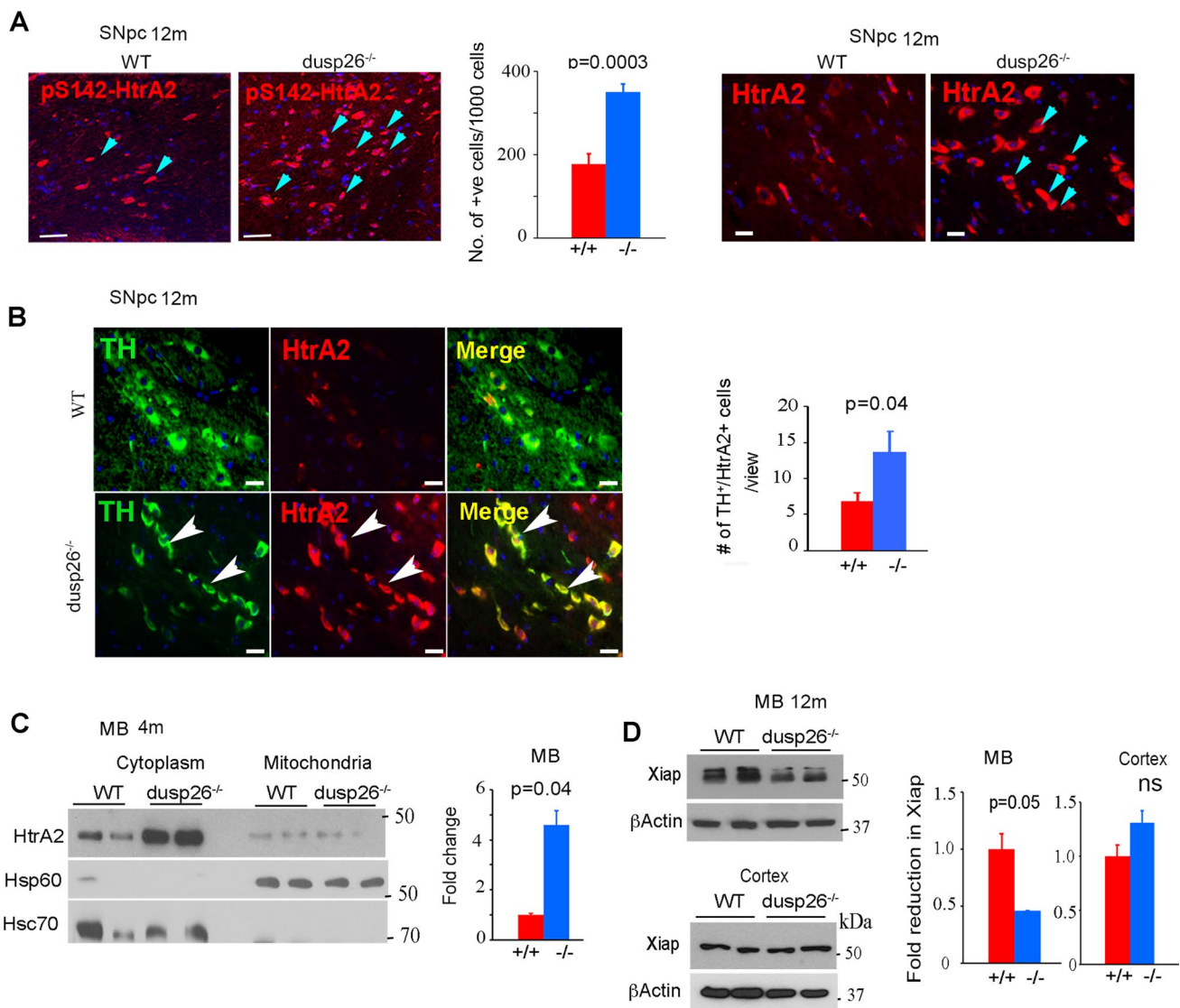
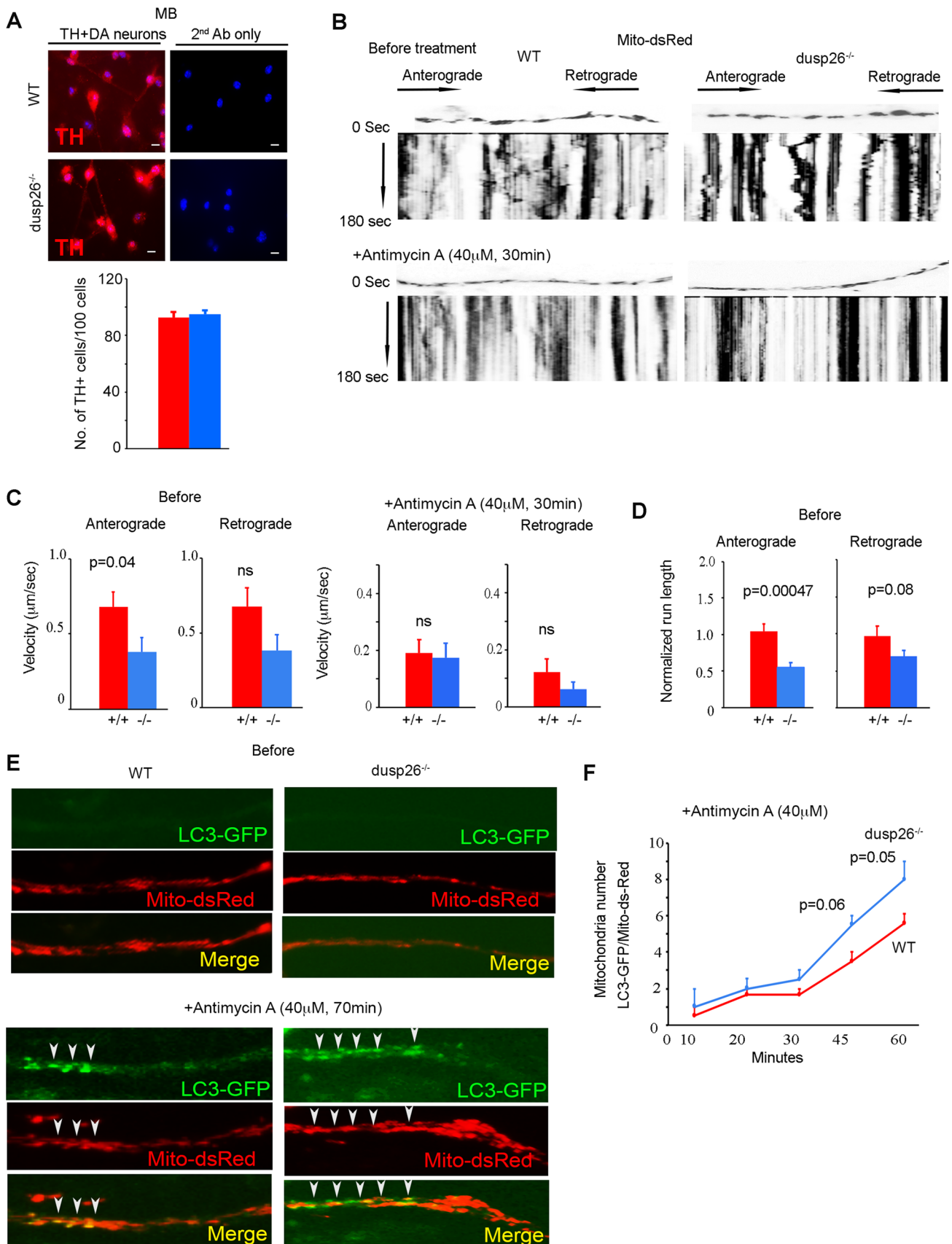


**Fig. 6** Increased expression and release of HtrA2 and p-HtrA2 from the mitochondria upon loss of Dusp26. **A** IHC staining of SNpc region showing expression of pS142-HtrA2 (left panel) or HtrA2 (right panel). Quantification of the number of p-HtrA2-positive cells per 1000 cells is presented.  $n=5$  mice/group. Scale bars p-HtrA2, 10  $\mu$ m, HtrA2, 20  $\mu$ m. **B** IHC staining of SNpc region showing colocalization of HtrA2 with TH in *dusp26*<sup>-/-</sup> mice. Quantification of the data is presented.  $n=5$  mice/group. Scale bars 20  $\mu$ m. **C** Immunoblotting analyses of MB cytoplasmic and mitochondrial fractions

showing the increased expression of HtrA2 in the cytoplasmic fraction isolated from the mutant mice. The expression of Hsp60 and Hsc70 indicate organelle purity. Quantification of the HtrA2 in the cytoplasmic fraction relative to WT is indicated in the right panel.  $n=4-5$  mice/group. **D** Immunoblotting analyses to detect Xiap expression in the MB and cortex of WT and *dusp26*<sup>-/-</sup> mice.  $\beta$ -actin is loading control. Quantification of the data relative to WT are presented in the right panel.  $n=4-5$  mice/group. In all relevant panels, bars are mean  $\pm$  SEM.  $p$  values are indicated in each panel

these MB neurons we performed live cell video microscopy to document mitochondrial motility following transfection of plasmids harboring Mito-dsRed that localizes in the mitochondria. The data presented in Fig. 7B–D indicate that *dusp26*<sup>-/-</sup> MB neurons exhibit significant reduction in velocity in the anterograde and less so in the retrograde direction as well as distance travelled along axons. In addition, studies indicate that mitochondrial movement is slowed down before the onset of mitophagy [55, 56].

Thus, to investigate whether changes in the mitochondrial motility leads to increased mitophagy in the absence of the *dusp26* gene, we cotransfected plasmids encoding LC3-GFP and Mito-dsRed in MB neurons [57]. The data indicate no significant accumulation of LC3-GFP in untreated neurons of both genotypes (Fig. 7E). However, mitochondria depolarization following treatment of neurons with 40  $\mu$ M Antimycin A, which is an inhibitor of mitochondrial oxidative phosphorylation and is known to reduce mitochondrial





◀ **Fig. 7** Reduced mitochondrial movement following loss of Dusp26. **A** Immunofluorescence analyses of cultured MB neurons using antibody to TH to show that the majority of cultured neurons are TH-positive DA neurons. Dapi is nuclear staining. Fluorescent-conjugated secondary antibody to show the absence of any non-specific staining. Bar 10  $\mu\text{m}$ . Quantification of TH-positive cells per total cells are indicated below. **B–D** Primary MB neurons were transfected with Mito-dsRed to detect mitochondrial movement before, or after treatment of neurons with 40  $\mu\text{M}$  Antimycin A for 30 min (**B**). The frame of each live imaging sequences is presented at the top of each kymograph that was generated from the movie. Position of the mitochondria is presented in the  $x$  axis and time is presented in the  $y$ -axis (0–180 s). Mitochondrial velocity before, and after addition of Antimycin A for 30 min are presented in **C**. Normalized mitochondrial run-length was quantified before any treatment (**D**). **E, F** Primary MB neurons were cotransfected with plasmids encoding Mito-dsRed and LC3-GFP. After 22 h, live cell imaging was performed. The intensity profile was generated using Image J before and 70 min after treatment of neurons with 40  $\mu\text{M}$  of antimycin A (lower panel) (**E**). Quantification of the mitochondria number in axons showing co-localization of Mito-dsRed and LC3-GFP in WT and *dusp26*<sup>-/-</sup> neurons using Image J (**F**) [57]. For each condition, more than 120 mitochondria in 3 separate cultures were analyzed. Data were averaged over at least  $n=10$  axons and 5 transfection experiments and statistical analyses was performed using Student's  $t$  test. In all relevant panels, bars are mean  $\pm$  SEM.  $p$  values are indicated in each panel. *ns* not significant

movement [57] resulted in significant increase in the number of mitochondria showing LC3-GFP puncta colocalizing with Mito-dsRed in *dusp26*<sup>-/-</sup> compared to WT (Fig. 7E, F). Taken together, the above data indicate that *dusp26*<sup>-/-</sup> MB neurons exhibit reduced motility in untreated cells and show increased numbers of mitochondria undergoing mitophagy when neurons are exposed to Antimycin A.

### Loss of dusp26 increases mitochondrial ROS production

As noted before, deletion of the *dusp26* gene in SH-SY5Y cells leads to increased ROS generation. Thus, we examined whether there is an increase in generation of ROS in the mitochondria of *dusp26*<sup>-/-</sup> MB neurons and whether it may contribute to the phenotype of *dusp26*<sup>-/-</sup> mice. We stained MB and STR/cortex cultured neurons with DHE or Mito-sox. Results show significant increases in the mitochondrial ROS levels in the MB neurons deficient in the *dusp26* gene relative to WT (Fig. 8A). There is also an increase in ROS levels in untreated STR/cortical neurons in the absence of Dusp26; however, the increase in mitochondria ROS levels did not reach a significant level.

To examine the cellular consequences due to the observed increases in the ROS levels, we assessed whether Dusp26 deletion increases ROS-induced DNA damage, which can be detected using 8-OHdG antibody. IHC staining analyses indicate significant increases in the level of 8-OHdG in cells located in the SNpc of *dusp26*<sup>-/-</sup> mice compared to WT (Fig. 8B). No significant 8-OHdG immunostaining

was observed in other regions of the CNS (e.g., cortex) (Fig. 8C). Additionally, increased levels of 8-OHdG in TH-positive DA neurons in the SNpc of *dusp26*<sup>-/-</sup> mice could be detected, which was not abundantly evident in WT littermates (Fig. 8D). The increases in ROS levels increased the mRNA levels of the major antioxidant enzymes SOD1 and iNOS and less significantly the SOD2 levels in the *dusp26*<sup>-/-</sup> MB and STR compared to WT suggesting a potential compensatory increase in the levels of these enzymes in the MB and STR of *dusp26*<sup>-/-</sup> mice (Fig. 8E). The above data indicate that loss of Dusp26 leads to increases in the mitochondrial ROS levels in the MB region and that is associated with ROS-induced DNA damage in DA neurons.

### Increased activation of MAP kinases in dusp26-deficient brain

Number of studies suggest that abnormal MAP kinase activation is linked to degeneration of neurons through activation of different signaling pathways. ROS is one of the major activators of MAP kinases in neurons [58]. Indeed, p38 and JNK kinases activation-associated neuronal cell death has been considered an important mechanism in brain pathology [59, 60]. To examine whether the increased generation of ROS in *dusp26*<sup>-/-</sup> neurons causes activation of MAP kinases, we determined the phosphorylation level of ERK1/2 (pT202/Y204), JNK1/2 (pT183/Y185), and p-p38 (pT180/Y182) MAP kinase in different brain regions (cortex, STR and MB) of *dusp26*<sup>-/-</sup> and WT mice. The phosphorylation levels of p-p38 increased in all the three brain regions of *dusp26*<sup>-/-</sup> mice, while p-ERK1/2 levels increased in cortex and STR, and p-JNK1/2 slightly but not significantly increased in the STR of *dusp26*<sup>-/-</sup> mice compared to WT mice (Fig. 9A–D). Interestingly, depending on the CNS region, similar to the increases observed in the p-p38 levels in *dusp26*<sup>-/-</sup> mice, there were increases in the pS207-MAP kinase kinase 6 (MKK6, active form) (Fig. 9A, B), which is the upstream kinase that phosphorylates p38 [61, 62]. The activation of p38 upstream kinase MKK6 may indicate that the increases in the phosphorylation of p38 in *dusp26*<sup>-/-</sup> brain tissue may be due to enhanced kinase activation signaling (e.g., ROS production due to loss of Dusp26). To further clarify whether the capacity of dephosphorylation of MAP kinases in *dusp26*<sup>-/-</sup> brain is impaired, we measured the mRNA expression levels of major MKPs, including Dusp1, 2, 4, 5, 8 and 10, which are known to dephosphorylate MAPKs in the nuclei and/or the cytoplasm. The expression of all the MKPs, with the exception of Dusp1 are comparable between WT and *dusp26*<sup>-/-</sup> MB region (Fig. 9E). Interestingly, loss of Dusp26 leads to a potential compensatory increase in Dusp1 mRNA levels in the MB region.

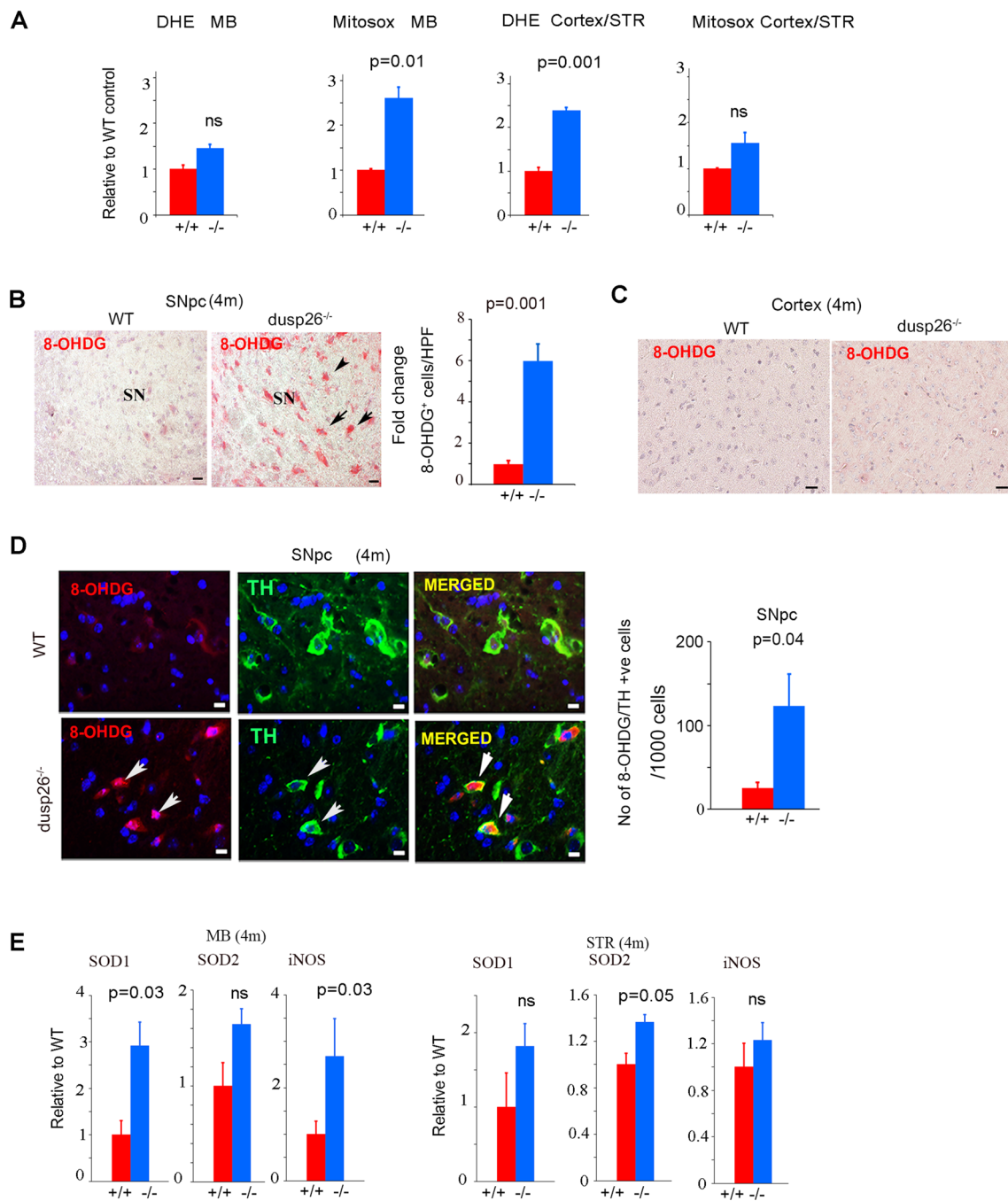


**Fig. 8** Increased ROS and ROS-induced DNA damage in DA neurons in the SNpc. **A** Untreated MB or cortex/STR primary neuronal cultures from WT and *dusp26*<sup>-/-</sup> mice were stained with 5 μM DHE or Mitoxox for 30 min followed by FACS analyses to determine the cytoplasmic or mitochondrial ROS levels, respectively. **B** IHC staining of SNpc showing 8-OHDG expression in 4-month-old WT and *dusp26*<sup>-/-</sup> mice. Tissue sections were stained with fast red to detect 8-OHDG-positive cells (arrows). Quantification of 8-OHDG-positive cells in SNpc is presented in the right panel. Scale bar 10 μm. *n*=5 mice/group. **C** IHC immunostaining of the cortical region of 4-month-old WT and *dusp26*<sup>-/-</sup> mice showing the absence of

8-OHDG accumulation. Scale bar 10 μm. *n*=5 mice/group. **D** Immunofluorescent staining showing coexpression of 8-OHDG and TH (arrows) in the SNpc in WT and *dusp26*<sup>-/-</sup> mice at 4 months of age. DAPI indicates nuclear staining. Quantification of 8-OHDG-positive cells expressing TH per 1000 cells (indicated by DAPI staining) is presented (right panel). Scale bar 10 μm. *n*=5 mice/group. **E** RT-qPCR analyses of MB and STR from WT and *dusp26*<sup>-/-</sup> mice to show the expression of genes relevant to increased ROS. *n*=5 mice/group. In all relevant panels, bars are mean ± SEM. *p* values are indicated in each panel. *ns* not significant

The IHC staining analyses confirmed that with respect to p-ERK1/2, p-JNK1/2 or p-p38, only p-p38 co-localized with TH-positive cells in the SNpc neurons of *dusp26*<sup>-/-</sup> mice, but not in WT (Fig. 9F, Fig. S3 and data not shown). The p-ERK1/2 were detected mainly in the cortex and less significantly in the Nucleus Accumbens (Fig. S3). It is of note that although we detected p-p38 in several areas of the brain following loss of Dusp26, we did not observe significant numbers of neuronal cell loss other than TH-positive cells in the SNpc in vivo. However, when STR/cortical neurons were treated with neurotoxin 6-OHDA, which causes cell death through inducing excessive ROS and subsequent activation of p38 [63–66], loss of Dusp26 increased the level of p-p38 and caspase 3 and neuronal cell death (Fig. 9G, H). The above result may suggest that the increased ROS levels following 6-OHDA treatment and/or the inability of Dusp26 to dephosphorylate p-p38 is the cause of the significant increased levels of p-p38 that is observed following loss of Dusp26.

The activation of MAP kinase pathway accompanied by the activation of inflammatory response in the brain of *dusp26*<sup>-/-</sup> mice that was demonstrated by (1) expansion of astrocytes (GFAP-positive cells) and microglia (Iba1-positive cells) in the MB region as early as 2 months of age and in the STR at 8–10 months of age (Fig. S4A–B), and (2) increases of pro-inflammatory cytokines (TNF $\alpha$ , IL1 $\beta$  and inf $\gamma$ ) in the MB and STR regions of *dusp26*<sup>-/-</sup> mice compared to WT was evident at 4 months of age (Fig. S4E).

In addition to the activation of p-p38 pathway, the activation of p53 by ROS is an important mechanism of inducing neuronal cell death [67, 68]. Studies also indicate that Dusp26 regulates the dephosphorylation of p-p53 [11, 12]. To test whether p53 pathway was regulated by loss of *dusp26* gene and contributed to induction of the knockout phenotype, we determined the expression of p53 and p-p53 in MB of *dusp26*<sup>-/-</sup> mice. Western blotting and IHC staining analyses indicated no significant increases in the expression levels of p53 or pS20-p53 in the TH-positive cells in the SNpc (Fig. S5). Furthermore, p53 target genes (Puma, Noxa, Bax, p21 and Notch) did not reveal any increases in their mRNA expression in the cortex or MB region from *dusp26*<sup>-/-</sup> mice compared to WT mice (Fig. S5). It is of note that although we were unable to detect p53 activity in DA neurons, it is possible that the rapid activation of p53 and its downstream targets such as Bax and the disappearance of dead cells cannot be ruled out.

Taken together, the above results suggest that Dusp26 loss leads to MAPK (including p-p38) activation in different brain regions but the p-p38 was specifically detected in the TH-positive DA neurons.

## Dusp26 forms complexes with phospho-p38 and core-kinase domain of LRRK2

As noted before, studies have revealed that in some cases Dusp26 requires a docking site or binding partner protein to perform its function [7, 10]. Here, we sought to identify the substrates of Dusp26 on the mitochondria and explore whether a binding partner protein is required for mitochondrial-associated function of Dusp26. Given the important role of p38 in neuronal cells survival and its activation in *dusp26*<sup>-/-</sup> neuron cells, we focused our studies on p38. First, we determined if Dusp26 interacts with endogenous p38 following ectopic expression of Dusp26 in HEK293 cells or whether the endogenous Dusp26 interacts with endogenous p-p38 (Fig. 10A, B). The interaction of Dusp26 with p38 and p-p38 suggests that p38 is a likely substrate of Dusp26 [69]. Since Dusp26 is detected on the OMM, we wanted to know if a fraction of p38 can also be detected in the mitochondrial fraction. Western blot analyses of cytosolic and mitochondrial fractions indicated that both p-p38 and p38 can be detected in both cytosolic and mitochondrial fractions (Fig. 10C). In addition, immunofluorescence analyses of endogenous Dusp26 and p-p38 in MB neurons indicated colocalization of the two proteins in specific areas (Fig. 10D, inset).

Interestingly, the leucine-rich repeat kinase 2 (LRRK2) has been shown to possess MAPKKK-like domain and activity [70]. Indeed, studies indicate that the Map kinase kinase 6 (MKK6), which is a MAPKKK substrate and is located upstream of p38 and phosphorylates p38 interacts with LRRK2 in the COR-kinase domain [71]. We also confirmed the interaction of MKK6 with LRRK2 following ectopic expression of these proteins in HEK293 cells (Fig. 10E). Both p38 and LRRK2 have been detected in the mitochondria or surface of the mitochondria, respectively [19, 57, 72]. As noted earlier, LRRK2 has been suggested to play a role as stress-activated protein scaffold controlling MAP kinase activity [71, 73]. Since Dusp26 may require a docking site for its function as we and others have reported [7, 10], we examined if Dusp26 can form complexes with LRRK2. Thus, we ectopically expressed Dusp26 and WT LRRK2, the LRRK2 encoding point mutations (G2019S or R1441G) or number of LRRK2 deletion mutants (ROC, COR, or ROC-COR-Kinase domains) in HEK293 cells (Fig. 10F, G). LRRK2 was pulled-down followed by western blotting to detect Dusp26. The data indicate that Dusp26 interacts with the full-length LRRK2 (Fig. 10G, lane 1). Interestingly, significant reductions in the ability of Dusp26 to interact with LRRK2 harboring G2019S or R1441G mutation was observed compared to WT LRRK2 (Fig. 10G, lanes 2–3,

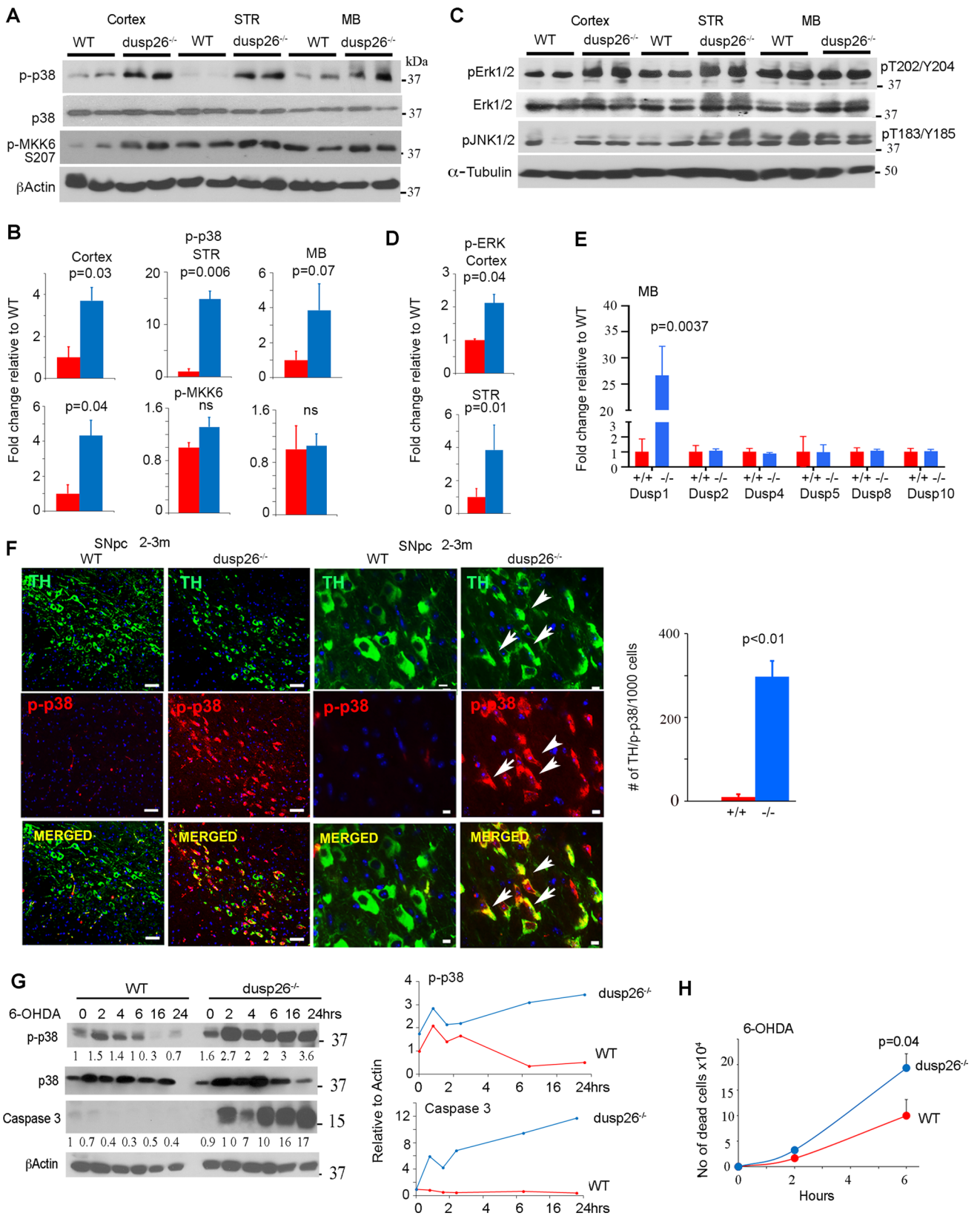


**Fig. 9** Dusp26 loss leads to MAPK activation in different brain regions including the TH-positive DA neurons. **A, B** Immunoblotting analyses of isolated cortex, STR and MB to detect the indicated proteins in 4-month-old WT and *dusp26*<sup>-/-</sup> mice.  $\beta$ -actin is loading control.  $n=4$  mice/group. Quantification of the immunoblots is indicated (**B**). **C, D** Immunoblotting analyses of isolated cortex, STR and MB to detect the indicated proteins in 4-month-old WT and *dusp26*<sup>-/-</sup> mice.  $\alpha$ -tubulin is loading control.  $n=4$  mice/group. Quantification of the p-ERK in cortex and STR is indicated (**D**). Increases in p-JNK1/2 in above brain regions were not significant. **E** RT-qPCR analyses to detect the expression of different Dusps in MB of WT and *dusp26*<sup>-/-</sup> mice. 2–3 months of age.  $n=5$  mice/group. **F** Immunofluorescent staining of SNpc region from WT and *dusp26*<sup>-/-</sup> mice showing coexpression of TH and p-p38 (arrows). Bars = 50  $\mu$ m left, and 5  $\mu$ m right panels. Quantification of TH and p-p38 -positive cells is presented in the right panel.  $n=5$  mice/group. **G, H** Cortical/STR neuronal cultures from WT and *dusp26*<sup>-/-</sup> mice were exposed to 6-OHDA (100  $\mu$ M) for the indicated hours. Cell lysates were analyzed by immunoblotting using the indicated antibodies.  $\beta$ -Actin is loading control. Quantification of a representative blot is indicated in the right panel. Cells in **H** were treated as in **G**, and number of dead cells were quantified using dye exclusion. In all relevant panels, bars are mean  $\pm$  SEM.  $p$  value is indicated in each panel

and Fig. 10H). It is of note that LRRK2 gene mutations in the G2019S and R1441G lead to increase kinase activity [74]. Since we observed that Dusp26 interaction with PD-related mutants of LRRK2 was reduced compared to WT, we considered the possibility that Dusp26 phosphatase activity could be reduced in cells expressing LRRK2 G2019S or R1441G mutant due to reduced binding of Dusp26 to these mutant forms of LRRK2. We, therefore, ectopically expressed Dusp26 as well as WT LRRK2 or LRRK2-G2019S or -R1441G in HEK293 cells as described in Fig. 10G. LRRK2 WT and mutants were pulled-down and Dusp26 phosphatase activity was determined. The data in the Fig. 10I indicate a significant reduction in Dusp26 phosphatase activity towards its substrate, P-Nitrophenyl Phosphate (PNPP) when LRRK2 mutants were used. In addition, we observed that Dusp26 interacts with the ROC-COR-kinase, as well as the COR and kinase domains of LRRK2 similar to what has been described for MKK6 binding to LRRK2 (Fig. 10F) [71].

To assess any potential changes in the expression of LRRK2 or phospho-LRRK2, we performed western blot analyses to detect their expression using whole cell lysates prepared from WT and *dusp26*<sup>-/-</sup> MB and STR regions. We observed increases in the pS935-LRRK2 in the MB, and less markedly in the STR upon loss of Dusp26, which suggested that LRRK2 may be more active in the absence of Dusp26 (Fig. 10J) [75]. No significant changes were observed in the expression of Miro, whose expression level has been shown to be affected by LRRK2 mutants [57]. Previous studies show that LRRK2 through interaction with Miro and Kif5

regulate mitochondrial motility [57]. Through phosphorylation of Kif5B/C/Kif1B, p-p38 also has been shown to slow down the mitochondrial motility [76–79]. Interestingly, all of Dusp26, Miro, and Kif1b could be co-immunoprecipitated with LRRK2, indicating that Dusp26 may form a complex with these proteins to regulate the mitochondria movement (Fig. 10K).

Taken together, our experiments show that Dusp26 interacts with p38, p-p38 and LRRK2 suggesting that LRRK2 may potentially serve as a scaffold or an upstream protein kinase for downstream signaling involving Dusp26 and p38 and their association with mitochondria (hypothetical model in Fig. S6).

### Dusp26-positive neurons in the healthy and PD patients

The above data indicate that the deletion of Dusp26 elicits neurodegenerative phenotype in our mouse model. We next asked whether Dusp26 is expressed in healthy and diseased PD human brain. First, we verified the expression of Dusp26 in normal human SNpc brain (Fig. 11A). Importantly, in this region, most of the Dusp26-expressing cells were TH-positive, indicating that Dusp26 expresses in DA neuron in human, consistent with the observation made in mouse brain (Fig. 11A). Next, we performed western blotting of healthy and PD patient SNpc brain region to detect TH. As expected, there is substantial reduction in TH in the brain of most PD patients (Fig. 11B). Interestingly, the average level of p-p38 in the PD patient samples increased compared to samples from healthy patients, indicating that activation of p38 pathway may contribute to the disease as previously reported [64, 66]. NeuN can be detected in most healthy and PD patient samples in immunoblotting, suggesting these SNpc samples in current studies were collected and preserved properly. In addition, we observed that the expression of molecular chaperone Hsc70 in PD brain samples was significantly increased, indicating the brains of these PD patients are under proteotoxic stress (e.g., oxidative stress). Together, the above data suggest that these PD patient samples collected in current study resemble *dusp26*<sup>-/-</sup> mouse brains in at least some molecular characteristics. Next, we examined the expression of Dusp26 in SNpc brain tissue sections by immunostaining. The significant reduction of Dusp26 expressing cells are presented in PD patients compared to healthy person (Fig. 11C–E). This is likely due to the loss of DA neurons that were positive for Dusp26. Of note, many neurons that are positive for Dusp26 contain neuromelanin, which is typical of catecholaminergic neurons of SNpc and loss of pigmentation in this region is one

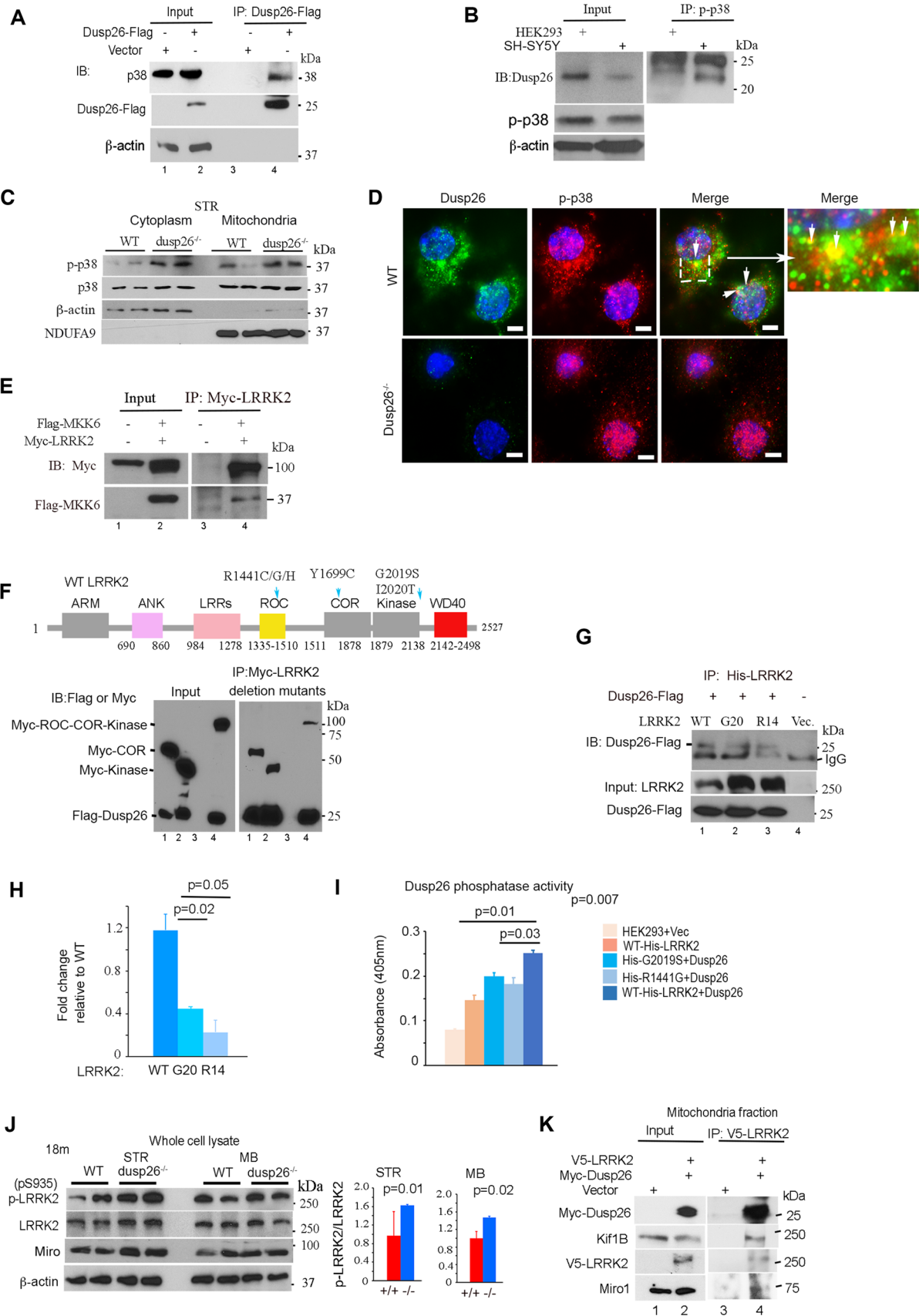


**Fig. 10** Dusp26 interacts with p38, LRRK2, Miro and Kif1B. **A** HEK293 cells were cotransfected with vector alone (lane 1) or expression plasmids encoding Dusp26-Flag (lanes 2). Dusp26-Flag was pulled down using antibody to Flag (lanes 3, 4) followed by immunoblotting to detect Dusp26-Flag and endogenous p38 (lanes 3, 4). **B** p-p38 was immunoprecipitated from HEK293 or SH-SY5Y cells and endogenous Dusp26 was detected by immunoblotting. Presence of relevant proteins in the input are indicated. **C** Immunoblot analyses of cytoplasmic and mitochondrial fractions isolated from STR of WT and *dusp26*<sup>-/-</sup> mice using antibodies to the indicated proteins.  $\beta$ -Actin is loading control. **D** Immunofluorescent analyses using antibodies to Dusp26 and p-p38 in the primary MB neurons prepared from WT and *dusp26*<sup>-/-</sup> mice. Merge shows colocalization of the two proteins in some areas. Scale bar 5  $\mu$ m. **E** HEK293 cells were transfected with plasmids encoding Flag-MKK6 (lane 2) and Myc-LRRK2 (ROC-COR-Kinase domain) (lanes 1, 2). Myc-LRRK2 was then pulled down using Myc antibody (lanes 3, 4) and complexes were immunoblotted to detect Flag-MKK6 and Myc-LRRK2. **F** Top panel: Schematic presentation of the full-length LRRK2 and location of different LRRK2 domains. Lower panel: HEK293 cells were cotransfected with plasmids encoding vector alone (lane 3) or Myc-LRRK2 deletion mutants (ROC-COR-Kinase, COR or Kinase domain) and Dusp26-Flag (lanes 1, 2, 4). Myc-LRRK2 was pulled-down followed by immunoblotting to detect Dusp26-Flag and Myc-LRRK2. Input presents the expression of LRRK2 mutants and Dusp26. **G, H** HEK293 cells were cotransfected with plasmids encoding full-length His-LRRK2 (WT) (lane 1), His-LRRK2 mutants G2019S, R1441G (lanes 2, 3) and Dusp26-Flag or vector alone (lane 4). His-LRRK2 was pulled down followed by immunoblotting to detect Dusp26 (lanes 1–4). Input shows the expression levels of His-LRRK2 in WT and mutants as well as Dusp26-Flag. Quantification of the data relative to WT LRRK2 is presented in **H**. **I** As in **G**, but following His-LRRK2 pulled-down, Dusp26 phosphatase activity was determined towards PNPP [7]. **J** Immunoblot analyses of whole cell lysates prepared from WT and *dusp26*<sup>-/-</sup> STR and MB were used to detect p-LRRK2, LRRK2 and Miro.  $\beta$ -Actin is loading control. Quantification of the p-LRRK2 expression to total LRRK2 is provided in the right panel. **K** HEK293 cells were transfected with vector alone (lane 1) or full-length V5-LRRK2 and Myc-Dusp26 (lane 2). LRRK2 was pulled-down from crude mitochondrial fraction using antibody to V5-LRRK2 followed by immunoblotting to detect Myc-Dusp26, V5-LRRK2 and endogenous Kif1B and Miro (lanes 3, 4). In all relevant panels, bars are mean  $\pm$  SEM. *p* values are indicated in each panel. All experiments were performed at least two times and in duplicates

of the characteristics observed in PD. Taken together, our data show that Dusp26 expression is significantly reduced in SNpc brain of PD patients compared to healthy brain.

## Discussion

The dual-specificity protein phosphatases (Dusps) play a critical cellular function by regulating signaling, thus affecting wide ranges of physiological activities. Aberrant Dusps activities have been documented in a number of human diseases, specifically through manipulation of MAP kinase signaling [3]. Mitochondria play a central role in the regulation of cell signaling and bioenergetics and its function is tightly regulated by variety of mechanisms,

including microenvironmental/local ion concentration alterations, oxygen/nutrients availability, and various cellular signaling pathways. Among these mechanisms, reversible phosphorylation of mitochondrial proteins regulated by kinases/phosphatases has gained significant attention in recent years. For example, upon exposure of cells to various stimuli or stressors, MAPKs are translocated to OMM to phosphorylate members of the Bcl-2 superfamily [19, 80–83]. While many kinases such as MAPKs, PINK1, LRRK2 and AMPK have proven to be critical for mitochondrial function, the function of mitochondria-associated phosphatases currently remain largely elusive. In the current study, we have provided evidence that Dusp26 is located on the OMM in neurons, neuroblastoma cells and HEK293 cells and that it is critical for maintaining normal mitochondrial homeostasis. Loss of Dusp26 leads to the impairment of mitochondrial respiration and increases in ROS production in both neurons and neuroblastoma cells. In addition to significant increases in the p-p38 in TH-positive neurons following loss of Dusp26, our data also show that Dusp26 can be co-immunoprecipitated with the phosphorylated form of p38 (Fig. 10B), suggesting that p38 is a likely substrate of Dusp26 associated with mitochondria and that it plays an important function on mitochondrial-associated p38 signaling. Another potential Dusp26 target is the pERK1/2 [7], which has also been shown to enter the mitochondria [72]. However, we did not co-localize ERK1/2 in TH-positive neurons in the SNpc (not shown). The p53 has also been shown to be a Dusp26 target, and when it enters the mitochondria results in cell death [84]. Although we were unable to detect p53 or p-p53 in vivo, the fact remains that the p53 is activated by ROS and causes cell death. Another known Dusp26 target is the adenylate kinase (AK2). AK2 is at least in part resides in the mitochondria and dephosphorylates FADD regulating cell proliferation [10]. Together, these studies suggest that Dusp26 may have number of substrates in cells. It is plausible to predict that Dusp26 regulates the dephosphorylation of multiple proteins going in or out of the mitochondria. Although, we detect the major portion of Dusp26 to be associated with the mitochondria fraction, we cannot rule out the possibility that this subcellular distribution pattern of Dusp26 in neurons will be the same in different cell types, especially in some cancer cells. Additional studies will be required to address the above questions.

As mentioned above, the N-terminal sequence of Dusp26 protein contains mitochondrial targeting sequence but that Dusp26 has no specific substrate binding domain. Therefore, in some cases, a binding partner protein that could provide a docking site or function as a scaffold protein for Dusp26 is required [7, 10]. In the current studies, we identified LRRK2 as a binding partner

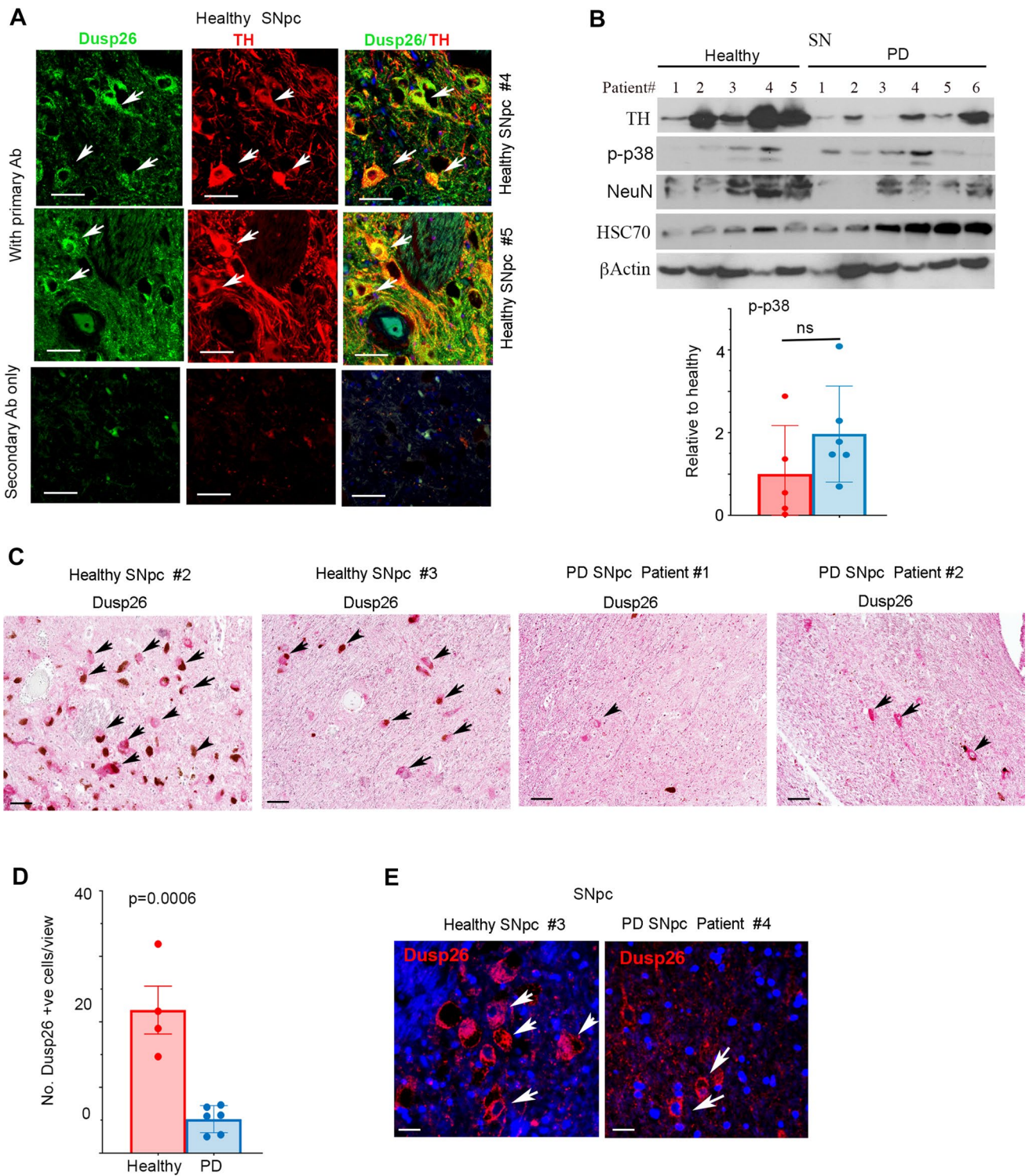


**Fig. 11** Dusp26 is expressed in TH-positive healthy human brain neurons in SNpc. **A** Immunofluorescent staining of SNpc obtained from healthy individuals using Dusp26 and TH antibodies. Merge shows colocalization of TH+/Dusp26+ neurons (arrows). Scale bar 50  $\mu$ m. **B** Immunoblot analyses of SNpc obtained from healthy and PD patients using the indicated antibodies.  $\beta$ -Actin is the loading control. Quantification of the p-p38 is presented in the lower panel. **C, D** IHC staining of Dusp26 in SNpc obtained from healthy and PD

patients. Quantification of the positive cells is presented in **D**. Bars are mean  $\pm$  SEM. *p* values are indicated in each panel. Scale bar 50  $\mu$ m. **E** Immunofluorescent staining of Dusp26 in SNpc obtained from healthy and PD patients. Positive cells are indicated by arrow. Scale bar 20  $\mu$ m. Experiments were performed with four healthy and six PD patient samples. In all relevant panels, bars are mean  $\pm$  SEM. *p* values are indicated in each panel



protein for Dusp26. Reduction of Dusp26 binding with LRRK2 significantly suppresses phosphatase activity of Dusp26 (Fig. 10I), indicating the importance of LRRK2 for Dusp26 function. LRRK2 has been shown to have MAPKKK activity and has been shown to bind MAPKK (MKK3, 6 and 7) [70, 71]. MKK6 is an upstream activator of p38 MAPK. Indeed, we do observe some increases in pS935-LRRK2, which is associated with its increased activity in the MB and STR and can be activated by ROS stimulating MKK6 and MAPK activity (e.g., p-p38) (Figs. 10J and S6 model). Although LRRK2 effects on MAPK is presumably small, in vivo LRRK2 generates a significant effect and MAPK activity is necessary for number of LRRK2 functions [71, 85]. The binding of Dusp26 with LRRK2 may also explain the alteration of mitochondria mobility that is observed in the *dusp26*<sup>-/-</sup> neurons (Fig. S6, model). It has been reported that LRRK2 is involved in regulating mitochondrial motility through its interaction with Miro and TRAK1/2 and kinesins. Phosphorylation of kinesins by p-p38 leads to detachment of Miro and TRAK1/2 from kinesins and LRRK2 and thereby affecting mitochondria movement [57, 76] (Fig. S6, model). In this study, we found that LRRK2 can be coimmunoprecipitated with Dusp26, Miro, and Kif1, indicating that Dusp26 may be located in these complexes. Dusp26 might regulate p38 activity through binding to LRRK2, regulating mitochondrial mobility (Fig. S6, model).

Because of high oxygen demand and abundance of lipid content, the brain is especially vulnerable to ROS-induced cell death. Oxidative stress has been suggested as a common etiology in various neurodegenerative diseases [27, 28]. For example, increased ROS in SNpc leads to DA neuronal death in PD patients [28, 86–88]. ROS has also been shown to control mitochondrial movement through ROS-induced p38 phosphorylation of kinesins [76]. The mitochondrial dysfunction and ROS generation is observed in SH-SY5Y cells and in *dusp26*<sup>-/-</sup> primary neurons isolated from postnatal day 18. This suggests that loss of Dusp26 results in an intracellular signaling imbalance initially observed in the postnatal period in the primary neurons irrespective of what comes later in vivo as animal ages (e.g., an increase in the inflammatory response). Although loss of Dusp26 and subsequent aberrant signaling does not result in death of primary neurons in vitro, additional impact of ROS and increased inflammatory response leads to death of mainly DA neurons which are more vulnerable to such stress signals in vivo. Of note, as cancer cells are normally more susceptible to cell death, we envision that cell death observed in SH-SY5Y cells that are deficient in Dusp26 does not exactly translate to the primary neurons in different brain regions other than the DA neurons. That may also extend to basal OCR that is increased in SH-SY5Y cells deficient in Dusp26 and

not in the *dusp26*<sup>-/-</sup> primary neurons compared to WT. Our findings suggest a new mechanism for ROS increase in the CNS and provides a potential clue for the therapy of neurodegenerative diseases. Activation of p38 has been recognized as a key component in PD pathogenesis [66, 89]. At least partially, p-p38 is localized in the mitochondria (Fig. 10 and [19, 72]) and p38 activation can result in neuronal cell death [63, 66]. In the in vivo models, p38 activation is often associated with microglia activation and neuroinflammation that can lead to the generation of additional factors that can lead to increased neuronal cell death. We envision that mitochondrial dysfunction and ROS generation are likely the earliest events, leading to the activation of MAPKs (e.g., p38) and the inflammatory response observed in different brain regions in vivo in *dusp26*<sup>-/-</sup> mice. The involvement of inflammation during the onset and progression of PD is clear; however, the triggering mechanism has not been identified. As we have presented here, it appears that aberrant inactivation of phosphatases such as OMM-associated Dusp26 and activation of kinases could be one triggering factor in the activation of inflammatory response that exacerbate with age [63, 64, 66, 68, 70, 71, 90–92]. Hence, ROS-p38 signaling may be the major contributor to the neuronal loss and inflammatory response in MB of *dusp26*<sup>-/-</sup> mice.

Based on our data, we propose that Dusp26 acts as a “guardian” that sits on the “gateway” (OMM) of mitochondria to monitor and regulate the signaling molecules, whose activation is regulated by reversible phosphorylation, while going in and out of the mitochondria or those residing on the OMM. Disturbances of the reversible phosphorylation that may occur in the mitochondria due to malfunction of Dusp26 might lead to dysregulation of mitochondrial function, such as impairment of mitochondria respiration, increases in ROS production and alterations of metabolism on context-dependent manner. Given that preferentially expressed in neuronal cells and some cancer cells, Dusp26 may play an important role in initiation and development of neurodegenerative disease and some cancers.

**Supplementary information** The online version contains supplementary material available at <https://doi.org/10.1007/s00018-022-04162-z>.

**Acknowledgements** Authors wish to thank Erin Eroglu for technical assistance. We also thank Drs. B. Lokeshwar and A. Terry and S. Naughton for providing valuable materials.

**Author contributions** BE performed experiments and analyzed data. XJ generated the mouse model and performed experiments and analyzed data and wrote the manuscript. SD, BO performed initial experiments. OAR analyzed data, DM and NFM, discuss results, designed experiments and wrote the manuscript.

**Funding** Research was supported by grants from NIHCA062130 and NIHCA132640 and in part by VA Merit Award 1101BX000161 (NFM).

**Availability of data and material** Upon publication, materials are available upon request.

## Declarations

**Conflict of interest** Authors declare no financial or non-financial interest.

**Ethical approval** All experiments involving mice were approved by Augusta University Institutional Animal Care and Use Committee (IACUC) in compliance with National Institutes of Health (NIH) guidelines.

**Human subject** Tissue specimens were generously provided by the NIH NeuroBank and Brain Tissue Repository. The materials were de-identified bio-specimens.

**Consent for publication** Not applicable.

## References

- Mustelin T, Vang T, Bottini N (2005) Protein tyrosine phosphatases and the immune response. *Nat Rev Immunol* 5:43–57. <https://doi.org/10.1038/nri1530>
- Patterson KI, Brummer T, O'Brien PM, Daly RJ (2009) Dual-specificity phosphatases: critical regulators with diverse cellular targets. *Biochem J* 418:475–489
- Thompson EM, Stoker AW (2021) A review of DUSP26: structure, regulation and relevance in human disease. *Int J Mol Sci*. <https://doi.org/10.3390/ijms22020776>
- Caunt CJ, Keyse SM (2013) Dual-specificity MAP kinase phosphatases (MKPs): shaping the outcome of MAP kinase signalling. *FEBS J* 280:489–504. <https://doi.org/10.1111/j.1742-4658.2012.08716.x>
- Pavic K, Duan G, Kohn M (2015) VHR/DUSP3 phosphatase: structure, function and regulation. *FEBS J* 282:1871–1890. <https://doi.org/10.1111/febs.13263>
- Russo LC, Farias JO, Ferruzo PYM, Monteiro LF, Forti FL (2018) Revisiting the roles of VHR/DUSP3 phosphatase in human diseases. *Clinics (Sao Paulo)* 73:e466s. <https://doi.org/10.6061/clinics/2018/e466s>
- Hu Y, Mivechi NF (2006) Association and regulation of heat shock transcription factor 4b with both extracellular signal-regulated kinase mitogen-activated protein kinase and dual-specificity tyrosine phosphatase DUSP26. *Mol Cell Biol* 26:3282–3294. <https://doi.org/10.1128/MCB.26.8.3282-3294.2006>
- Vasudevan SA, Nuchtern JG, Shohet JM (2005) Gene profiling of high risk neuroblastoma. *World J Surg* 29:317–324. <https://doi.org/10.1007/s00268-004-7820-7>
- Yu W et al (2007) A novel amplification target, DUSP26, promotes anaplastic thyroid cancer cell growth by inhibiting p38 MAPK activity. *Oncogene* 26:1178–1187. <https://doi.org/10.1038/sj.onc.1209899>
- Kim H et al (2014) The DUSP26 phosphatase activator adenylate kinase 2 regulates FADD phosphorylation and cell growth. *Nat Commun* 5:3351. <https://doi.org/10.1038/ncomms4351>
- Shi Y et al (2015) NSC-87877 inhibits DUSP26 function in neuroblastoma resulting in p53-mediated apoptosis. *Cell Death Dis* 6:e1841. <https://doi.org/10.1038/cddis.2015.207>
- Shang X et al (2010) Dual-specificity phosphatase 26 is a novel p53 phosphatase and inhibits p53 tumor suppressor functions in human neuroblastoma. *Oncogene* 29:4938–4946. <https://doi.org/10.1038/onc.2010.244>
- Jung S et al (2016) Dual-specificity phosphatase 26 (DUSP26) stimulates Abeta42 generation by promoting amyloid precursor protein axonal transport during hypoxia. *J Neurochem* 137:770–781. <https://doi.org/10.1111/jnc.13597>
- Wang JY, Lin CH, Yang CH, Tan TH, Chen YR (2006) Biochemical and biological characterization of a neuroendocrine-associated phosphatase. *J Neurochem* 98:89–101. <https://doi.org/10.1111/j.1471-4159.2006.03852.x>
- Tanuma N et al (2009) Protein phosphatase Dusp26 associates with KIF3 motor and promotes N-cadherin-mediated cell-cell adhesion. *Oncogene* 28:752–761. <https://doi.org/10.1038/onc.2008.431>
- Huang F, Sheng X-X, Zhang H-J (2019) DUSP26 regulates podocyte oxidative stress and fibrosis in a mouse model with diabetic nephropathy through the mediation of ROS. *BBRC* 515:410–416
- Armes JE et al (2004) Candidate tumor-suppressor genes on chromosome arm 8p in early-onset and high-grade breast cancers. *Oncogene* 23:5697–5702. <https://doi.org/10.1038/sj.onc.1207740>
- Pribill I et al (2001) High frequency of allelic imbalance at regions of chromosome arm 8p in ovarian carcinoma. *Cancer Genet Cytogenet* 129:23–29
- Lucero M, Suarez AE, Chambers JW (2019) Phosphoregulation on mitochondria: Integration of cell and organelle responses. *CNS Neurosci Ther* 25:837–858. <https://doi.org/10.1111/cns.13141>
- Rardin MJ, Wiley SE, Murphy AN, Pagliarini DJ, Dixon JE (2008) Dual specificity phosphatases 18 and 21 target to opposing sides of the mitochondrial inner membrane. *J Biol Chem* 283:15440–15450. <https://doi.org/10.1074/jbc.M709547200>
- Giorgianni F, Koirala D, Weber KT, Beranova-Giorgianni S (2014) Proteome analysis of subarcolemmal cardiomyocyte mitochondria: a comparison of different analytical platforms. *Int J Mol Sci* 15:9285–9301. <https://doi.org/10.3390/ijms15069285>
- Kruse R, Hojlund K (2017) Mitochondrial phosphoproteomics of mammalian tissues. *Mitochondrion* 33:45–57. <https://doi.org/10.1016/j.mito.2016.08.004>
- Padrao AI, Vitorino R, Duarte JA, Ferreira R, Amado F (2013) Unraveling the phosphoproteome dynamics in mammal mitochondria from a network perspective. *J Proteome Res* 12:4257–4267. <https://doi.org/10.1021/pr4003917>
- Triplett JC et al (2015) Quantitative expression proteomics and phosphoproteomics profile of brain from PINK1 knockout mice: insights into mechanisms of familial Parkinson's disease. *J Neurochem* 133:750–765. <https://doi.org/10.1111/jnc.13039>
- Pagliarini DJ, Dixon JE (2006) Mitochondrial modulation: reversible phosphorylation takes center stage? *Trends Biochem Sci* 31:26–34. <https://doi.org/10.1016/j.tibs.2005.11.005>
- Michel PP, Hirsch EC, Hunot S (2016) Understanding dopaminergic cell death pathways in Parkinson disease. *Neuron* 90:675–691. <https://doi.org/10.1016/j.neuron.2016.03.038>
- Singh A, Kukreti R, Saso L, Kukreti S (2019) Oxidative stress: a key modulator in neurodegenerative diseases. *Molecules* 24(8):1583. <https://doi.org/10.3390/molecules24081583>
- Kim GH, Kim JE, Rhie SJ, Yoon S (2015) The role of oxidative stress in neurodegenerative diseases. *Exp Neurobiol* 24:325–340. <https://doi.org/10.5607/en.2015.24.4.325>
- Shadel GS, Horvath TL (2015) Mitochondrial ROS signaling in organismal homeostasis. *Cell* 163:560–569. <https://doi.org/10.1016/j.cell.2015.10.001>
- Eroglu B, Moskophidis D, Mivechi NF (2010) Loss of Hsp110 leads to age-dependent tau hyperphosphorylation and early accumulation of insoluble amyloid beta. *Mol Cell Biol* 30:4626–4643. <https://doi.org/10.1128/MCB.01493-09>
- Dimauro I, Pearson T, Caporossi D, Jackson MJ (2012) A simple protocol for the subcellular fractionation of skeletal muscle

- cells and tissue. *BMC Res Notes* 5:513. <https://doi.org/10.1186/1756-0500-5-513>
32. Chatterjee A et al (2016) MOF acetyl transferase regulates transcription and respiration in mitochondria. *Cell* 167:722–738 e723. <https://doi.org/10.1016/j.cell.2016.09.052>
  33. Thomas B, von Coelln R, Mandir AS, Trinkaus DB, Farah MH, Lim KL, Calingasan NY, Bea MF, Dawson VL, Dawson TM (2007) MPTP and DSP-4 susceptibility of substantia nigra and locus coeruleus catecholaminergic neurons in mice is independent of parkin activity. *Neurobiol Dis* 26:312–322
  34. Neumann S, Chassefeyre R, Campbell GE, Encalada SE (2017) KymoAnalyzer: a software tool for the quantitative analysis of intracellular transport in neurons. *Traffic* 18:71–88. <https://doi.org/10.1111/tra.12456>
  35. Spinazzi M, Casarin A, Pertegato V, Salviati L, Angelini C (2012) Assessment of mitochondrial respiratory chain enzymatic activities on tissues and cultured cells. *Nat Protoc* 7:1235–1246. <https://doi.org/10.1038/nprot.2012.058>
  36. Jha P, Wang X, Auwerx J (2016) Analysis of mitochondrial respiratory chain supercomplexes using blue native polyacrylamide gel electrophoresis (BN-PAGE). *Curr Protoc Mouse Biol* 6:1–14. <https://doi.org/10.1002/9780470942390.mo150182>
  37. Sotnikova TD et al (2005) Dopamine-independent locomotor actions of amphetamines in a novel acute mouse model of Parkinson disease. *PLoS Biol* 3:e271. <https://doi.org/10.1371/journal.pbio.0030271>
  38. Wang Y, Zheng Y, Nishina PM, Naggert JK (2009) A new mouse model of metabolic syndrome and associated complications. *J Endocrinol* 202:17–28
  39. Claros MG, Vincens P (1996) Computational method to predict mitochondrially imported proteins and their targeting sequences. *Eur J Biochem* 241:779–786
  40. Deas E, Plun-Favreau H, Wood NW (2009) PINK1 function in health and disease. *EMBO Mol Med* 1:152–165. <https://doi.org/10.1002/emmm.200900024>
  41. Zhou C et al (2008) The kinase domain of mitochondrial PINK1 faces the cytoplasm. *Proc Natl Acad Sci USA* 105:12022–12027. <https://doi.org/10.1073/pnas.0802814105>
  42. Sacco F et al (2014) Combining affinity proteomics and network context to identify new phosphatase substrates and adapters in growth pathways. *Front Genet* 5:115. <https://doi.org/10.3389/fgene.2014.00115>
  43. Chen HH, Luche R, Wei B, Tonks NK (2004) Characterization of two distinct dual specificity phosphatases encoded in alternative open reading frames of a single gene located on human chromosome 10q22.2. *J Biol Chem* 279:41404–41413. <https://doi.org/10.1074/jbc.M405286200>
  44. Madamanchi NR, Runge MS (2007) Mitochondrial dysfunction in atherosclerosis. *Circ Res* 100:460–473. <https://doi.org/10.1161/01.RES.0000258450.44413.96>
  45. Jankovic J (2008) Parkinson's disease: clinical features and diagnosis. *J Neurol Neurosurg Psychiatry* 79:368–376. <https://doi.org/10.1136/jnnp.2007.131045>
  46. Jenner P et al (2013) Parkinson's disease—the debate on the clinical phenomenology, aetiology, pathology and pathogenesis. *J Parkinsons Dis* 3:1–11. <https://doi.org/10.3233/JPD-130175>
  47. Tang FL et al (2015) VPS35 deficiency or mutation causes dopaminergic neuronal loss by impairing mitochondrial fusion and function. *Cell Rep* 12:1631–1643. <https://doi.org/10.1016/j.celrep.2015.08.001>
  48. Itoh K, Nakamura K, Iijima M, Sesaki H (2013) Mitochondrial dynamics in neurodegeneration. *Trends Cell Biol* 23:64–71. <https://doi.org/10.1016/j.tcb.2012.10.006>
  49. Plun-Favreau H et al (2007) The mitochondrial protease HtrA2 is regulated by Parkinson's disease-associated kinase PINK1. *Nat Cell Biol* 9:1243–1252. <https://doi.org/10.1038/ncb1644>
  50. Alnemri ES (2007) HtrA2 and Parkinson's disease: think PINK? *Nat Cell Biol* 9:1227–1229. <https://doi.org/10.1038/ncb1107-1227>
  51. Hegde R et al (2002) Identification of Omi/HtrA2 as a mitochondrial apoptotic serine protease that disrupts inhibitor of apoptosis protein-caspase interaction. *J Biol Chem* 277:432–438. <https://doi.org/10.1074/jbc.M109721200>
  52. Kieper N et al (2010) Modulation of mitochondrial function and morphology by interaction of Omi/HtrA2 with the mitochondrial fusion factor OPA1. *Exp Cell Res* 316:1213–1224. <https://doi.org/10.1016/j.yexcr.2010.01.005>
  53. Verhagen AM et al (2002) HtrA2 promotes cell death through its serine protease activity and its ability to antagonize inhibitor of apoptosis proteins. *J Biol Chem* 277:445–454. <https://doi.org/10.1074/jbc.M109891200>
  54. Vande Walle L, Lamkanfi M, Vandenabeele P (2008) The mitochondrial serine protease HtrA2/Omi: an overview. *Cell Death Differ* 15:453–460. <https://doi.org/10.1038/sj.cdd.4402291>
  55. Ashrafi G, Schlehe JS, LaVoie MJ, Schwarz TL (2014) Mitophagy of damaged mitochondria occurs locally in distal neuronal axons and requires PINK1 and Parkin. *J Cell Biol* 206:655–670. <https://doi.org/10.1083/jcb.201401070>
  56. Wang X et al (2011) PINK1 and Parkin target Miro for phosphorylation and degradation to arrest mitochondrial motility. *Cell* 147:893–906. <https://doi.org/10.1016/j.cell.2011.10.018>
  57. Hsieh CH et al (2016) Functional impairment in Miro degradation and mitophagy is a shared feature in familial and sporadic Parkinson's disease. *Cell Stem Cell* 19:709–724. <https://doi.org/10.1016/j.stem.2016.08.002>
  58. Son Y et al (2011) Mitogen-activated protein kinases and reactive oxygen species: how can ROS activate MAPK pathways? *J Signal Transduct* 2011:792639. <https://doi.org/10.1155/2011/792639>
  59. Tong H et al (2018) Simvastatin inhibits activation of NADPH oxidase/p38 MAPK pathway and enhances expression of antioxidant protein in Parkinson disease models. *Front Mol Neurosci* 11:165. <https://doi.org/10.3389/fnmol.2018.00165>
  60. Jiang G et al (2014) Gastrodin protects against MPP(+)-induced oxidative stress by up regulates heme oxygenase-1 expression through p38 MAPK/Nrf2 pathway in human dopaminergic cells. *Neurochem Int* 75:79–88. <https://doi.org/10.1016/j.neuint.2014.06.003>
  61. Gallo KA, Johnson GL (2002) Mixed-lineage kinase control of JNK and p38 MAPK pathways. *Nat Rev Mol Cell Biol* 3:663–672. <https://doi.org/10.1038/nrm906>
  62. Kim EK, Choi EJ (1802) Pathological roles of MAPK signaling pathways in human diseases. *Biochim Biophys Acta* 2010:396–405. <https://doi.org/10.1016/j.bbadis.2009.12.009>
  63. Choi WS et al (2004) Phosphorylation of p38 MAPK induced by oxidative stress is linked to activation of both caspase-8- and -9-mediated apoptotic pathways in dopaminergic neurons. *J Biol Chem* 279:20451–20460. <https://doi.org/10.1074/jbc.M311164200>
  64. Correa SA, Eales KL (2012) The role of p38 MAPK and its substrates in neuronal plasticity and neurodegenerative disease. *J Signal Transduct* 2012:649079. <https://doi.org/10.1155/2012/649079>
  65. Wang G, Pan J, Chen SD (2012) Kinases and kinase signaling pathways: potential therapeutic targets in Parkinson's disease. *Prog Neurobiol* 98:207–221. <https://doi.org/10.1016/j.pneurobio.2012.06.003>
  66. Jha SK, Jha NK, Kar R, Ambasta RK, Kumar P (2015) p38 MAPK and PI3K/AKT signalling cascades in Parkinson's disease. *Int J Mol Cell Med* 4:67–86
  67. Karunakaran S et al (2008) Selective activation of p38 mitogen-activated protein kinase in dopaminergic neurons of substantia nigra leads to nuclear translocation of p53 in 1-methyl-4-phenyl-1,2,3,6-tetrahydropyridine-treated mice. *J Neurosci* 28:12500–12509. <https://doi.org/10.1523/JNEUROSCI.4511-08.2008>

68. Gomez-Lazaro M et al (2008) 6-Hydroxydopamine activates the mitochondrial apoptosis pathway through p38 MAPK-mediated, p53-independent activation of Bax and PUMA. *J Neurochem* 104:1599–1612. <https://doi.org/10.1111/j.1471-4159.2007.05115.x>
69. Vasudevan SA et al (2005) MKP-8, a novel MAPK phosphatase that inhibits p38 kinase. *Biochem Biophys Res Commun* 330:511–518. <https://doi.org/10.1016/j.bbrc.2005.03.028>
70. Gloeckner CJ, Schumacher A, Boldt K, Ueffing M (2009) The Parkinson disease-associated protein kinase LRRK2 exhibits MAPKKK activity and phosphorylates MKK3/6 and MKK4/7, in vitro. *J Neurochem* 109:959–968. <https://doi.org/10.1111/j.1471-4159.2009.06024.x>
71. Hsu CH et al (2010) MKK6 binds and regulates expression of Parkinson's disease-related protein LRRK2. *J Neurochem* 112:1593–1604. <https://doi.org/10.1111/j.1471-4159.2010.06568.x>
72. Hotamisligil GS, Davis RJ (2016) Cell signaling and stress responses. *Cold Spring Harb Perspect Biol*. <https://doi.org/10.1101/cshperspect.a006072>
73. Liou AK, Leak RK, Li L, Zigmond MJ (2008) Wild-type LRRK2 but not its mutant attenuates stress-induced cell death via ERK pathway. *Neurobiol Dis* 32:116–124. <https://doi.org/10.1016/j.nbd.2008.06.016>
74. Cookson MR (2015) LRRK2 pathways leading to neurodegeneration. *Curr Neurol Neurosci Rep* 15:42. <https://doi.org/10.1007/s11910-015-0564-y>
75. Wallings R, Manzoni C, Bandopadhyay R (2015) Cellular processes associated with LRRK2 function and dysfunction. *FEBS J* 282:2806–2826. <https://doi.org/10.1111/febs.13305>
76. Debattisti V, Gerencser AA, Saotome M, Das S, Hajnoczky G (2017) ROS control mitochondrial motility through p38 and the motor adaptor Miro/Trak. *Cell Rep* 21:1667–1680. <https://doi.org/10.1016/j.celrep.2017.10.060>
77. Morfini GA et al (2013) Inhibition of fast axonal transport by pathogenic SOD1 involves activation of p38 MAP kinase. *PLoS One* 8:e65235. <https://doi.org/10.1371/journal.pone.0065235>
78. Tanaka K, Sugiura Y, Ichishita R, Mihara K, Oka T (2011) KLP6: a newly identified kinesin that regulates the morphology and transport of mitochondria in neuronal cells. *J Cell Sci* 124:2457–2465. <https://doi.org/10.1242/jcs.086470>
79. Nangaku M et al (1994) KIF1B, a novel microtubule plus end-directed monomeric motor protein for transport of mitochondria. *Cell* 79:1209–1220
80. Chambers JW, Cherry L, Laughlin JD, Figuera-Losada M, Lograsso PV (2011) Selective inhibition of mitochondrial JNK signaling achieved using peptide mimicry of the Sab kinase interacting motif-1 (KIM1). *ACS Chem Biol* 6:808–818. <https://doi.org/10.1021/cb200062a>
81. Wiltshire C, Matsushita M, Tsukada S, Gillespie DA, May GH (2002) A new c-Jun N-terminal kinase (JNK)-interacting protein, Sab (SH3BP5), associates with mitochondria. *Biochem J* 367:577–585. <https://doi.org/10.1042/BJ20020553>
82. Putcha GV et al (2003) JNK-mediated BIM phosphorylation potentiates BAX-dependent apoptosis. *Neuron* 38:899–914. [https://doi.org/10.1016/s0896-6273\(03\)00355-6](https://doi.org/10.1016/s0896-6273(03)00355-6)
83. Dhanasekaran DN, Reddy EP (2008) JNK signaling in apoptosis. *Oncogene* 27:6245–6251. <https://doi.org/10.1038/onc.2008.301>
84. Marchenko ND, Zaika A, Moll UM (2000) Death signal-induced localization of p53 protein to mitochondria. A potential role in apoptotic signaling. *J Biol Chem* 275:16202–16212. <https://doi.org/10.1074/jbc.275.21.16202>
85. Plowey ED, Cherra SJ 3rd, Liu YJ, Chu CT (2008) Role of autophagy in G2019S-LRRK2-associated neurite shortening in differentiated SH-SY5Y cells. *J Neurochem* 105:1048–1056. <https://doi.org/10.1111/j.1471-4159.2008.05217.x>
86. Gaki GS, Papavassiliou AG (2014) Oxidative stress-induced signaling pathways implicated in the pathogenesis of Parkinson's disease. *NeuroMol Med* 16:217–230. <https://doi.org/10.1007/s12017-014-8294-x>
87. Tieu K, Ischiropoulos H, Przedborski S (2003) Nitric oxide and reactive oxygen species in Parkinson's disease. *IUBMB Life* 55:329–335. <https://doi.org/10.1080/1521654032000114320>
88. Yang S, Lian G (2020) ROS and diseases: role in metabolism and energy supply. *Mol Cell Biochem* 467:1–12. <https://doi.org/10.1007/s11010-019-03667-9>
89. Mathiasen JR et al (2004) Inhibition of mixed lineage kinase 3 attenuates MPP+-induced neurotoxicity in SH-SY5Y cells. *Brain Res* 1003:86–97. <https://doi.org/10.1016/j.brainres.2003.11.073>
90. Pajares M, Rojo AI, Manda G, Boscá L, Cuadrado A (2020) Inflammation in Parkinson's disease: mechanisms and therapeutic implications. *Cells* 9:1687. <https://doi.org/10.3390/cells9071687>
91. Chen J et al (2018) Phosphorylation of Parkin at serine 131 by p38 MAPK promotes mitochondrial dysfunction and neuronal death in mutant A53T alpha-synuclein model of Parkinson's disease. *Cell Death Dis* 9:700. <https://doi.org/10.1038/s41419-018-0722-7>
92. Culbert AA et al (2006) MAPK-activated protein kinase 2 deficiency in microglia inhibits pro-inflammatory mediator release and resultant neurotoxicity. Relevance to neuroinflammation in a transgenic mouse model of Alzheimer disease. *J Biol Chem* 281:23658–23667. <https://doi.org/10.1074/jbc.M513646200>

**Publisher's Note** Springer Nature remains neutral with regard to jurisdictional claims in published maps and institutional affiliations.